Climate Dynamics (2024) 62:9565–9585
https://doi.org/10.1007/s00382-024-07411-y

ORIGINAL ARTICLE

Tropical and mid-latitude causal drivers of the eastern Mediterranean Etesians during boreal summer

G. Di Capua[1,2] · E. Tyrlis[3,4] · D. Matei[4] · R. V. Donner[1,2]

Received: 26 January 2024 / Accepted: 18 August 2024 / Published online: 31 August 2024
© The Author(s) 2024

Abstract
During boreal summer, large scale subsidence and a persistent northerly flow, known as the Etesians, characterize the tropospheric circulation over the eastern Mediterranean. The Etesians bring clear skies and alleviate the impact of heat waves over the region. The intraseasonal variability of the Etesians and subsidence over the eastern Mediterranean has been thought to be influenced by the South Asian monsoon and atmospheric processes over the North Atlantic. Here, we employ causal effect networks and causal maps, obtained by applying the Peter and Clark Momentary Conditional Independence (PCMCI) causal discovery algorithm, to identify causal precursors of Etesians. We find that both wave train activity over the North Atlantic/North American region and convective activity over South Asia associated with the Indian summer monsoon (ISM) are causally related to the Etesians at 3-day time scale. Thus, intraseasonal ISM variability affects the eastern Mediterranean circulation, though its influence is conveyed via a Middle East ridge. On longer weekly time scale, the mid-latitude influence weakens, while the influence of the tropical convective activity via the Middle East ridge remains stable. Moreover, the heat low over the Arabian Peninsula, a feature strongly responsible for the development of the Etesians, is caused by a stronger Middle East ridge and not by North Atlantic wave activity. Finally, we discuss potential implication for circulation changes in the eastern Mediterranean due to anthropogenic global warming.

Keywords Indian monsoon · Mediterranean · Etesians · Mid-latitude wave train

1 Introduction

During boreal summer, northerly winds known as the "Etesians", are a key feature of the low-level tropospheric circulation over the eastern Mediterranean (Tyrlis and Lelieveld 2013). At intraseasonal time scales, the variability related to the Etesians is important to determine climate features and weather conditions in the region. The Etesians are accompanied by the advection of colder air masses originating over eastern Europe to the Balkans and the Middle East, thus mitigating surface air temperatures in the affected region and preventing the formation of heat waves during the summer season (Metaxas and Bartzokas 1994; Founda and Santamouris 2017). However, this cooling effect is partly offset by clear sky conditions and adiabatic warming related to subsidence throughout the tropospheric column, which accompany strong episodes of Etesians. Intense winds and dry conditions can create favourable conditions for the ignition and propagation of wild fires (Paschalidou and Kassomenos 2016). Air quality in the region is also affected by the Etesians, as their ventilation effect can disperse air pollution and increase air quality of urban areas (Kanakidou et al. 2011; Rizos et al. 2022). The Etesians also play a role in influencing remote systems such as the Sahel monsoon system (Raicich et al. 2003; Gaasbeek et al. in review).

The Etesians are associated to prevailing northerlies in the lower troposphere (between 1000 and 850 hPa) over the eastern Mediterranean (31°–40° N, 22°–28° E) between June and September (Tyrlis and Lelieveld 2013). The climatological average velocity of the Etesians over the Aegean is about

✉ G. Di Capua
dicapua@pik-potsdam.de

1 Earth System Analysis, Potsdam Institute for Climate Impact Research, Member of the Leibniz Association, Potsdam, Germany

2 Department of Water, Environment, Construction and Safety, Magdeburg-Stendal University of Applied Sciences, Magdeburg, Germany

3 Department of Physics, National and Kapodistrian University of Athens, Athens, Greece

4 Max Planck Institute for Meteorology, Hamburg, Germany

5 m s^{-1} (depending on the exact region, month(s) and pressure level considered). The Etesians peak between July and August, coinciding with the most active phase of the Indian summer monsoon (ISM). These northerlies arise due to an east–west low-level sea level pressure gradient between the western Mediterranean, featuring a semi-permanent seasonal high pressure, and the Middle East, characterized by the Persian heat low. The seasonal Persian trough emerges as the westward extension of the surface low pressure system that is the dominant climatological feature over the Indian subcontinent and the Arabian Sea. The intraseasonal variability of winds in the region is characterized by periods of enhanced northerlies lasting from a few days up to 10–15 days, called *outbreaks* of Etesians (Tyrlis and Lelieveld 2013). During outbreak of Etesians events, daily (absolute) wind speed can reach values of 8–9 m s^{-1} over the Aegean.

The variability of the Etesians is associated with local and remote drivers depending on the time scale analysed (Tyrlis and Lelieveld 2013). Previous research has shown that while local phenomena such as the amplification of surface diabatic heating over the Middle East intensifies the Etesians at daily time scales (diurnal cycle), remote phenomena such as North Atlantic wave disturbances and the ISM convective activity can affect these winds at both intraseasonal and seasonal time scales (Tyrlis and Lelieveld 2013; Tyrlis et al. 2015). The influence of mid-latitude circulation on the Etesians is characterized by synoptic disturbances leading to the development of an anticyclone centred over central Europe that precedes the onset of outbreaks of Etesians by 2–4 days. When the ridge shifts over the Balkans, cold air advection on its eastern flank triggers an outbreak, and the low level wind switches from south-westerlies to north-easterlies (Tyrlis and Lelieveld 2013).

At seasonal time scales, the background northerlies associated with the Etesians can be explained by the presence of deep monsoon convection over the Indian peninsula (Tyrlis et al. 2013). Despite being located about 50° to the east and 20° to the south, convective activity during the ISM season (June to September) produces a heat source which can trigger Rossby waves to the west and affect tropospheric circulation in remote regions by causing subsidence in Northern Africa and over the eastern Mediterranean (Rodwell and Hoskins 1996; Cherchi et al. 2014). The exact latitudinal position of the heating source over the ISM region is relevant in determining the nature of the response: when the heating source is located near the equator, the Rossby wave response weakens, while a heating source located over the Bay of Bengal produces a stronger Rossby wave response that reaches North Africa (Rodwell and Hoskins 2001). The ISM system exhibits its own intraseasonal variability, which is characterized by periods of enhanced rainfall over central India (active phases) and periods with reduced precipitation (break phases) (Gadgil and Joseph 2003; Rajeevan et al. 2010). An oscillation between the equatorial Indian ocean and the Indian subcontinent is also detected on time scales of about 30–60 days (Kulkarni et al. 2011), which combined with the Madden Julian oscillation appears as the boreal summer intraseasonal oscillation (BSISO) (Jiang et al. 2004; Kikuchi et al. 2012). Hence, the exact latitudinal location of convective activity related to the ISM varies on time scales of a few weeks, thus modulating the monsoon-desert mechanism and its influence on the circulation over the Mediterranean and North Africa at intraseasonal time scales. The monsoon–desert mechanism, i.e. a teleconnection connecting enhanced ISM convection to enhanced subsidence in North Africa and the eastern Mediterranean (Rodwell and Hoskins 1996), is also relevant in the context of climate change, as precipitation is projected to increase over India under global warming scenarios (Wang et al. 2020; Katzenberger et al. 2021), which would then imply an intensification of the subsidence over North Africa (Cherchi et al. 2016).

Beside exploiting dynamical models, the monsoon–desert mechanism has been studied also from a statistical point of view in observational datasets by assessing the causality behind the relationship between tropical convective activity and mid-latitude circumglobal wave activity on 2D causal maps (Di Capua et al. 2020b). Di Capua et al. (2020b) highlights the causal pathway from the ISM region towards North Africa, which manifests as a positive causal effect of strong convective activity on the geopotential heights at 200 hPa (Z200) field of North Africa. The causal influence of the ISM extends also to the mid-latitude belt and the interaction with the circumglobal teleconnection (CGT) pattern is depicted both in causal effect networks between meaningful scalar index variables of specific spatio-temporal patterns and 2D causal maps (Di Capua et al. 2020a, b). In particular, the CGT index, defined as Z200 averaged over the eastern side of the Caspian Sea (35–40° N, 60–70° E), acts as doorway between the tropical belt and the mid-latitude region (Di Capua et al. 2020a). In addition to the aforementioned remote drivers, local diabatic enhancement mechanisms have also been hypothesized to be playing a role, together with dynamical features related to the orography of the region (Tyrlis et al. 2013). In contrast to the monsoon – desert mechanism, which implies the propagation of a wave disturbance, but not the transport of air masses, some studies have proposed that the Etesians are part of a Walker type closed circulation cell, which would imply a transport of air masses from the ISM region toward the eastern Mediterranean (Ziv et al. 2004).

The Mediterranean basin and its surrounding regions represent a hot spot for current and future climate change (Seager et al. 2014; Barcikowska et al. 2020; Vogel et al. 2020). Rising temperatures, changes in atmospheric circulation patterns and soil moisture availability can pose

severe threats to society, economy and ecology of the region (Hochman et al. 2022). Future projections from the coupled model inter-comparison project phase 6 (CMIP6) suggests a drying of the Mediterranean region. Accompanied by increasing surface air temperatures, this drying trend represents a challenging issue for water availability, increases the chance of wildfires, poses a threat to agricultural yields and can have a negative impact on tourism in the region (Ruffault et al. 2018; Grillakis 2019; Morán-Ordóñez et al. 2020). More frequent and/or severe drought events can also contribute to deteriorating fragile political equilibria, which may provide more favourable conditions for conflicts in the affected area (Kelley et al. 2015; Schleussner et al. 2016). In addition, more frequent and/or intense heat waves have a negative effect on mortality in the region, especially in countries where sustainable adaptation measures are not yet available (Gasparrini et al. 2017). In this context, changes in the intraseasonal and interannual variability of the Etesians, given their link to surface air temperature over the eastern Mediterranean region, can impact heat waves and wildfires frequency in the region. In the past decades, a downward trend has been recorded in the intensity and frequency of outbreaks of the Etesians (Poupkou et al. 2011). Future projections anticipate that the Etesians will strengthen again under global warming scenarios, mainly caused by a strengthening of the high pressure over Balkans (Ezber 2019).

While previous work has primarily addressed the influence of North Atlantic atmospheric variability on daily Etesians (Tyrlis et al. 2013), the causal pathways which govern the intraseasonal variability of the Etesians have not yet been identified. Moreover, the effect of tropical mechanisms such as the ISM convective activity, has been hypothesize to act at seasonal time scales. However, Di Capua et al. (2020b, 2023) have shown that an effect of ISM convective activity on North Africa can be detected also at weekly time scales. Thus, different intraseasonal time scales may be dominated by different drivers. In this study we aim to assess the following aspects: (i) quantify the impact of tropical and extra-tropical drivers on the eastern Mediterranean circulation, (ii) assess the physical mechanisms behind such causal pathways, and (iii) disentangle local from remote influences on the conditions leading to strong Etesians.

Assessing causality between different atmospheric and surface phenomena and distinguishing between spurious correlations and true causal links from sets of observational time series is a challenging task. Sophisticated causal discovery algorithms, such as the Peter and Clark Momentary Conditional Independence (PCMCI) algorithm, go beyond commonly used bivariate statistical association measures, like correlation, as well as classical bivariate measures of causality, like Granger causality, which do not take into consideration the possible effect of any third variables. Accordingly, PCMCI and its algorithmic variants provide valuable tools to identify and separate true causal from spurious links and quantify the causal effect of each component of the system on all its other elements (Runge et al. 2014, 2019; Runge 2018). PCMCI has been applied to a growing number of physical phenomena and has demonstrated its usefulness in identifying local and remote causal pathways both in tropical and extra-tropical systems (Kretschmer et al. 2016; Di Capua et al. 2020a). Some of its most recent application include studies on stratospheric polar vortex variability (Kretschmer et al. 2016, 2017, 2018), Atlantic hurricane activity (Pfleiderer et al. 2020), interdecadal variability of the Silk Road pattern (Stephan et al. 2019), tropical–extra-tropical interactions in the Northern Hemisphere (Di Capua et al. 2020b, a), seasonal statistical forecasting for US surface temperatures (Vijverberg et al. 2020; Vijverberg and Coumou 2022) and for Moroccan crop yields (Lehmann et al. 2020) as well as model evaluation (Nowack et al. 2020; Di Capua et al. 2023).

To answer the aforementioned research questions, here we apply the PCMCI causal discovery algorithm to both, sets of time series representative for the phenomena of interest and then on 2D climatological fields. In the remainder of this manuscript, we first describe the data and method used (Sect. 2), then present the results obtained (Sect. 3) and finally discuss the results (Sect. 4).

2 Data and methods

2.1 Data

We analyse intraseasonal (3-day and 7-day time scales) tropical convective activity and mid-latitude circulation during the extended boreal summer period (June to September, JJAS) using gridded data ($0.25° \times 0.25°$ spatially averaged to $1° \times 1°$) for the period 1979–2022 from the ERA5 reanalysis dataset (Hersbach et al. 2020) provided by the European Centre for Medium-range Weather Forecasts (ECMWF). Specifically, we consider daily (temporally averaged to obtain 3-day and 7-day samples) geopotential height at 200 hPa (Z200), outgoing longwave radiation (OLR), mean sea level pressure (MSLP), temperature at 500 hPa (T500), meridional wind component (V-wind), vertical wind (W-wind) and potential temperature (Θ) at several pressure levels. Θ is obtained from temperature and pressure fields (see text T1 in the Supplementary Material). Z200 fields are most suitable to identify wave activity in the mid-latitudes, while OLR fields represent a good proxy of convective activity in the tropics, with convective high cloud tops being represented by negative OLR anomalies.

Each extended summer season (June to September, JJAS) consists of 40 (17) time steps for the 3-day (7-day) time scale, resulting in a total of 40 (17) × 44 years = 1760 (748) time steps. The climatological cycle and long-term trend are removed in each time step for all field and indices used (unless otherwise specified). Moreover, the seasonal mean values for each variable are also removed from the time series, to ensure that the interannual variability is removed and that intraseasonal relationships are detected. These steps ensure that the input time series are thus made of detrended anomalies centred around zero, as required by the causal discovery algorithm detailed in the following.

A proxy for the intensity of the Etesians, referred hereafter as Etesians index, and the target variable of interest, is defined as the 3-days meridional wind field at 850 hPa (V850) averaged over the region 30°–41° N, 22°–28° E (magenta box in Fig. 1a) and reverted in sign (i.e. northerly anomalies have a positive sign).

2.2 Causal discovery method

In general, simple (simultaneous or lagged) correlation can quantify the existence of concurrent behaviour between pairs of time series in the sense of a linear functional dependency. However, simple correlation cannot be used to infer causality. To identify causal relationships between the Etesians and other atmospheric fields, here we apply the Peter and Clark Momentary Conditional Independence (PCMCI) algorithm (Runge 2018; Runge et al. 2019). PCMCI uses iterative conditioning to identify and remove spurious statistical associations between pairs of time series, here called *actors*, and thus identify the true *causal* links (where the term causal rests on a series of assumptions, and it is valid only within the specific set of time series analysed). For more details see Runge (2018).

PCMCI can use both linear or nonlinear bivariate dependency measures to identify and quantify causal links.

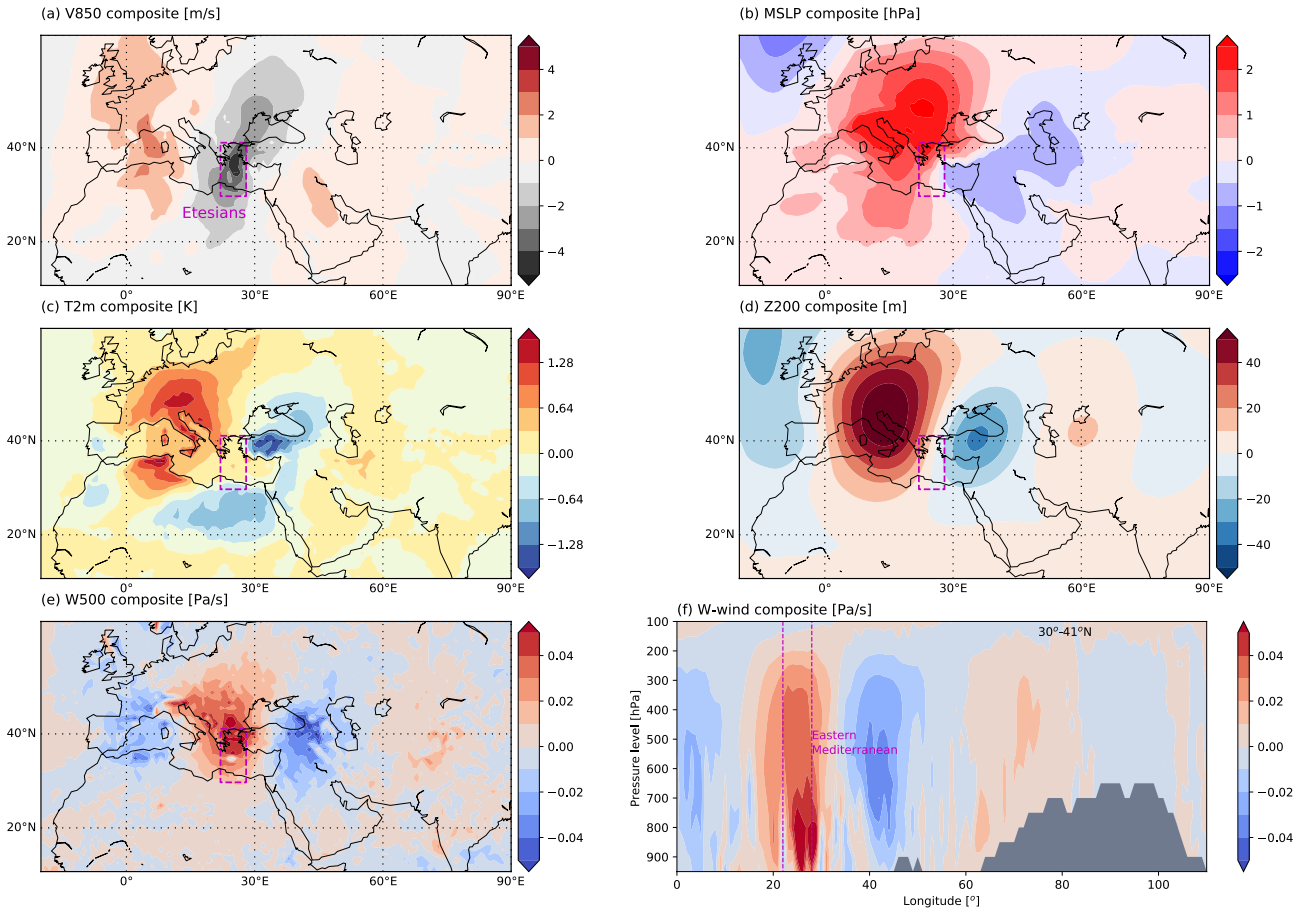

Fig. 1 Characteristic circulation features of the Etesians (3-day time scale). Panel **a** shows the ERA5 V850 composites for time steps which exceed the + 1 s.d. threshold of the Etesians index time series for the period 1979–2022. The Etesians are defined as the spatial average of V850 meridional wind over the magenta box area (30°–41° N, 22°–28° E) for summer (JJAS). Panels **b**–**e**: Same as for panel **a** but for the MSLP, T2m, Z200 and W500 fields respectively. Panel **f** same as panel **a** but for W-wind between the 950 hPa and the 100 hPa levels averaged over the latitudinal Sect. 22°–28° N. For W-wind and W850, red shading represents subsidence while blue shading represent ascent

Here, we employ PCMCI under the assumption of linearity, hence applying the concept of partial correlation to build the subsequent analysis upon. Linearity here means that each actor will be expressed as a linear combination of the identified set of causal parents. While nonlinear measures may better represent the behaviour of the atmospheric circulation, which intrinsically exhibits nonlinearities, we are limited here by the number of available time steps in our reanalysis dataset, which may be insufficient for obtaining stable estimates of nonlinear conditional association measures. Therefore, applying a nonlinear measure of conditional dependence is not feasible here. Nevertheless, linearity assumptions have proven valid in first order and found to often provide reasonable approximation (Hlinka et al. 2014).

PCMCI consists of two steps, the PC-step and the MCI-step. In the PC-step, the algorithm first identifies for each actor j in the set P, e.g. $P = \{A, B, C, D, E\}$, a sub-set P_j^0 by selecting those actors in P which are significantly correlated with j at a certain lag τ and at a certain predefined threshold significance level α. These actors form the initial set of potential "parents" (i.e. direct predictors) of j, e.g. for actor A we have $P_A^0 = \{A_{t=-1}, B_{t=-2}, E_{t=-1}, D_{t=-3}\}$. Each further iteration i will then check whether the partial correlation between $A_{t=0}$ and each of its potential parents in P_A^{i-1} is still significant when $A_{t=0}$ and this potential parent are linearly regressed on a sub-set of P_A^{i-1}, e.g. for $i = 1$, the partial correlation between $A_{t=0}$ and $A_{t=-1}$ conditioned on $B_{t=-2}$ will be expressed as:

$$\rho(A_{t=0}, A_{t=-1}|B_{t=-2}) = \rho(Res(A_{t=0}), Res(A_{t=-1})) \quad (1)$$

where $Res(A_{t=0})$ are the residuals of $A_{t=0}$ after removing the linear influence of $B_{t=-2}$ and $Res(A_{t=-1})$ are the residuals of $A_{t=-1}$ after removing the linear influence of $B_{t=-2}$. When the number of actors in P_A^{i-1} equals i, the algorithm converges and the set of parents for the next actors is calculated. At the end of the PC-step, each actor will have its own set of parents, and these will enter the second step of the algorithm.

In the MCI-step, the partial correlation between each possible pair of actors is calculated by regressing *once* on the combined set of parents. For example, assuming that $P_A^2 = \{A_{t=-1}, B_{t=-2}, E_{t=-1}\}$ and $P_B^3 = \{D_{t=-1}, B_{t=-1}\}$, the partial correlation between $A_{t=0}$ and $B_{t=-1}$ will be

$$\rho(A_{t=0}, B_{t=-1}|A_{t=-1}, B_{t=-2}, E_{t=-1}, D_{t=-2}), \quad (2)$$

where the lags of P_B^3 are adjusted by adding the lag of $B_{t=-1}$. After checking all pairs of actors, the final set of causal parents for each actor are identified and the causal effect coefficient, called the β coefficient (or β-value for short), is calculated by linearly regressing each parent on its set of causal parents. For example, assuming that the set of causal parents of $A_{t=0}$ is $P_A^2 = \{A_{t=-1}, B_{t=-2}, E_{t=-1}\}$, then the β coefficient of the causal link $B_{t=-2} \rightarrow A_{t=0}$ will be the coefficient $\beta_{B_{t=-2}}$ from the multivariate linear regression:

$$A_{t=0} = \beta_{A_1} * A_{t=-1} + \beta_{B_2} * B_{t=-2} + \beta_{E_1} * E_{t=-1} + \xi$$

where ξ represents the error of the linear regression. Thus, when actors are standardized, e.g. $\beta_{B_2} = 0.55$ means that A at lag 0 will increase by 0.55 standard deviations (s.d.) for a 1 s.d. increase of B at lag -2.

The causal links obtained in PCMCI are then graphically represented in a causal effect network (CEN), where circles (i.e., the nodes of the network) represent the actors, and the edges of the arrows represent the direction of causality. The colour of the edges (nodes) represents the strength of the causal link, i.e. the β coefficient (respectively, the auto-β coefficient measuring the time-delayed self-influence of an actor). Note that when the same causal link is detected multiple times at different time lags, the colour of the arrow shows the strength of the link with the maximum (absolute) β-value.

In addition to CENs for individual target variables (time series), we also use PCMCI for the estimation of causal maps. Here, a set of CENs is estimated from the available data, in which a number of actors n are fixed, i.e. they are present in all CENs, while exactly one remaining actor represents the time series of a certain atmospheric field at a specific grid point (determined by its latitude and longitude). By performing the analysis for all grid points individually, the resulting β coefficients of each CEN can be plotted on a map at the location of the respective grid point. Thus, the concept of causal maps resembles that of correlation maps but instead of the correlation coefficient, the value at each grid point represents the β coefficient of a specific causal link. For further details, we refer to Di Capua et al. (2020a).

The significance threshold adopted in this work for plotting the results for both CEN and correlation maps is $\alpha = 0.05$ where all p-values have been adjusted by applying the Benjamini–Hochberg false discovery rate (FDR) correction to control for multiple testing among the multiple grid locations in the causal maps (Benjamini and Hochberg 1995).

3 Results

3.1 Potential precursors of the Etesians

The JJAS distribution of the Etesians index at 3-day time scale has a mean value of 4.2 m s^{-1} and a standard deviation (s.d.) of 2.1 m s^{-1}. Composites of the V850 field, for periods of enhanced Etesians, i.e. time steps for

which the Etesians index positive deviation from its mean exceeds 1 s.d., are shown in Fig. 1a. Here, the Etesians are visible as northerly wind anomalies expanding from eastern Europe to northeast Africa and peaking over the Aegean Sea during June, July, August and September. The composite for MSLP field during periods of enhanced Etesians is shown in Fig. 1b. An east–west oriented MSLP gradient arises over the Mediterranean basin. In the west, positive MSLP anomalies, centred over Italy and the Balkans, extend to the northeast towards eastern Europe and in the south towards Libya. In the east, negative MSLP anomalies are located over the Middle East region. The composite for T2m field shows higher temperature anomalies over Italy and the Balkans and lower temperature anomalies over the Caspian Sea, Turkey, the western Middle East and eastern North Africa (Fig. 1c), respectively in correspondence of the positive and negative MSLP anomalies shown in Fig. 1b. At higher levels, this circulation pattern is only partly barotropic: composites for Z200 fields during enhanced Etesians are shown in Fig. 1d and reveal a positive Z200 anomaly over Italy and the Balkans (in correspondence to the high MSLP anomaly located in the same region) and a negative anomaly over Turkey and the Black Sea. The latter is however not centred over the Middle East, as it is the case for the negative MSLP anomaly.

Composites for vertical velocity at 500 hPa (W500) during enhanced Etesians are shown in Fig. 1e. Ascending motions (negative W500 anomalies) are found over the western Mediterranean, extending from Algeria towards Spain and Southern France, and over the Middle East, the Caspian Sea and the Black Sea. Descending motions (positive W500 anomalies) are shown over the Aegean Sea and the eastern Mediterranean, in correspondence with the Etesians (magenta box in Fig. 1e). Note that the locations of ascending and descending motions are not centred together with those of the high- and low-pressure systems shown in Fig. 1d. Descending motions over the eastern Mediterranean are also shown in the vertical cross-section for the composites of W-wind fields at different isobaric levels during enhanced Etesians (Fig. 1f). Ascending motions are depicted to the east and the west of the region of subsidence.

The full JJAS climatology of each of these fields plus those for the vertical cross-section of V-wind, W-wind, OLR and the meridional wind at 10 m (V10m) are shown in Fig. S1 in the Supplementary Material. Here, the total climatological values for each field are shown, without any detrending. The most prominent climatological features over the Mediterranean and South Asia are (i) the ISM low linked to the Persian trough over the Arabian Peninsula (Fig. S1c), (ii) the background northerlies, i.e. the Etesians, over the eastern Mediterranean which appear in the V850, V10m and V-wind climatologies (Fig. S1a, b, g), (iii) the widespread subsidence over the eastern Mediterranean (Fig. S1e, f), (iv) the Tibetan anticyclone over northern India and the Tibetan Plateau (Fig. S1d) and (v) the ISM convective activity centred over the Bay of Bengal and central India (Fig. S1h). The same composites as for Fig. 1 but for the weekly (7-day average) time scale are shown in Fig. S2 in the Supplementary Material. Qualitatively, the same patterns are shown, though with a lower magnitude of the anomalies, as expected in composites obtained at a longer time scale.

The evolution of the atmospheric patterns that precede and follow enhanced Etesians are analysed by calculating correlation maps between the Etesians index and the MSLP and Z200 fields at different lags, i.e. from lag − 2 to lag + 2 (in units of 3-day time steps, see Fig. 2a–e and f–j respectively). At lag 0, the east–west pressure gradient shown in Fig. 1c is reproduced by positive correlation coefficients over the western Mediterranean and negative correlation coefficients over the Middle East (Fig. 2c). The Persian trough is identified by a blue contour line labelled as "Pers-trough" in Fig. 2c, where the blue contour is drawn at a correlation value r = − 0.25 (see Table 1). A time series with the same name is created by averaging the MSLP over the Persian trough region. Similar to Fig. 1c, a wave pattern is identified in the Z200 correlation maps at lag 0 extending from the eastern North Atlantic to the Caspian Sea (Fig. 2h). This pattern shows a low (negative correlation coefficients) over the eastern North Atlantic and a low over the Black Sea corresponding to periods of enhanced Etesians. Two highs (positive correlation coefficients) are depicted centred over Italy and extending between the eastern Mediterranean Sea and the Arabian Peninsula (Fig. 2h). Both MSLP and Z200 correlation maps show a wave pattern appearing at lag − 1 over the North Atlantic (Fig. 2b, g) and propagating towards Eurasia in the following time steps, reaching South Asia at lag + 2 (Fig. 2e, j). The wave pattern emerging over the North Atlantic and western Europe at lag − 1 in the Z200 correlation map (blue box in Fig. 2g) is identified as a potential precursor of the Etesians. The corresponding time series (NAtl-wave, Table 1) is obtained by calculating the spatial correlation between the pattern shown in the blue box in Fig. 2g and the Z200 fields: for each time step a correlation coefficient represents how strong the NAtl-wave is. Over the Middle East, a region of positive correlation at lag − 1 is shown. This region is selected as the third potential driver of the variability of the Etesians (on intraseasonal timescales) and its time series (ME-ridge) is calculated by averaging Z200 over the area bound by the highlighted contours (blue contour line in Fig. 1g, see Table 1).

Next, the correlation between the NAtl-wave index and Z200 is calculated and the evolution of the mid-latitude wave is depicted from lag − 2 to lag + 2 (Fig. 2k–o). The wave is already visible at lag − 2, showing a negative centre

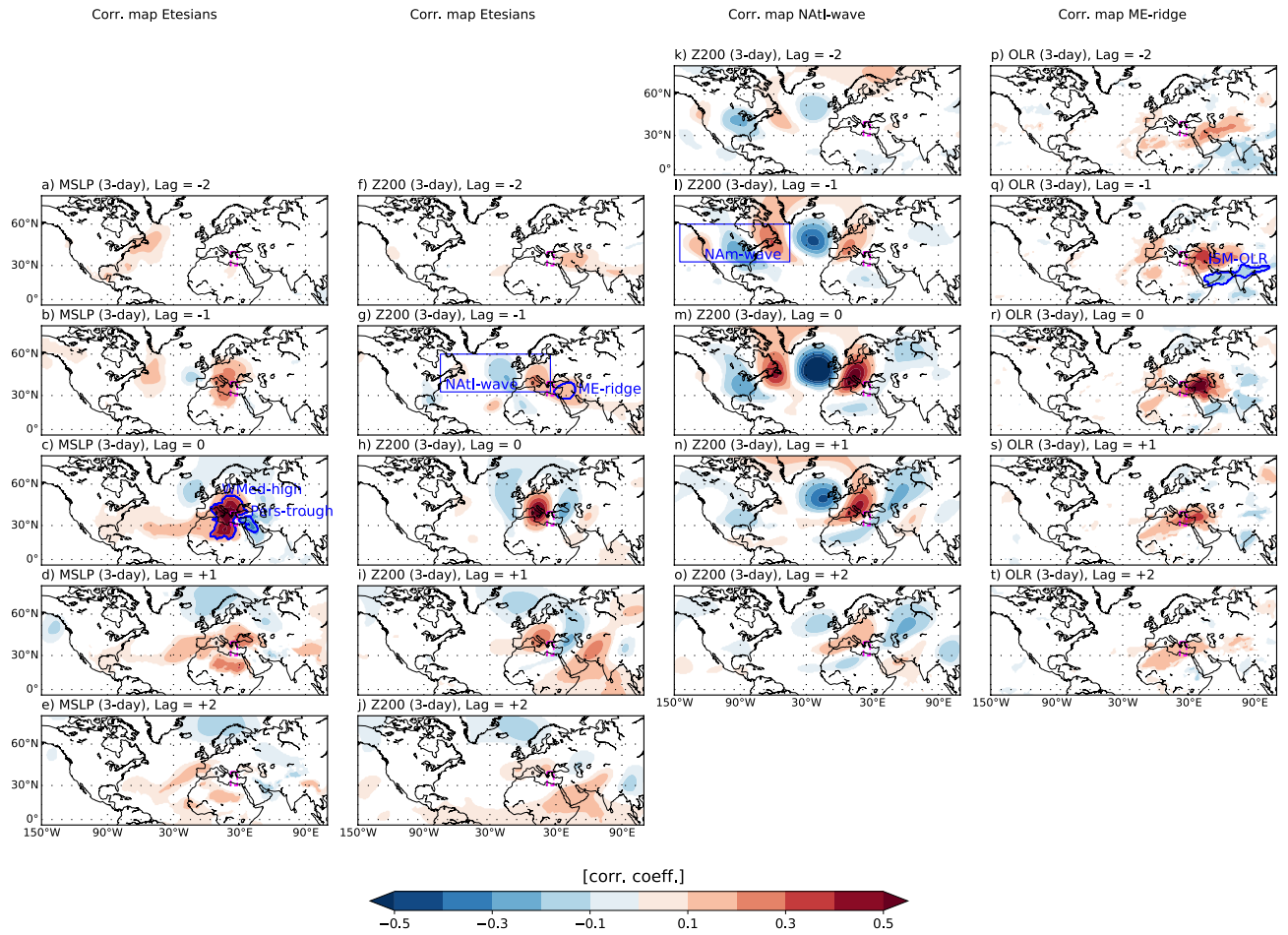

Fig. 2 Potential precursors of the Etesians. Panel **a** shows the correlation map between the Etesians index time series and the MSLP field at lag − 2 (3-day time steps). Panels **b**–**e** same as panel **a** but for lag − 1 to + 2. Panels **f**, **g** same as for panels **a**–**e** but for Z200 fields. Panels **k**–**o** same as for panels **a**–**e** but for the correlation between the NAtl-wave and the Z200 fields. Panels **p**–**t** same as for panels **a**–**e** but for the correlation between the ME-ridge and the OLR fields. Grid points for which the correlation is not significant at $\alpha < 0.05$ (after applying the Benjamini–Hochberg correction) are shown in white. Note that lag 0 shows the correlation between variable x and field y taken contemporaneously. Negative lags show correlation between variable x and field y where the time line for field y is shifted backward by a number of time steps n equal to the shown lag. The opposite is true for positive lags, where variable x precedes field y. Also note that lag 0 in the two right columns corresponds to lag − 1 in the two left columns

Table 1 Potential precursors

Short name	Long name	Region	Method
Etesians index	Etesian index	30–41° N, 22–28° E	V850 spatial average
Pers. Trough	Persian Trough	Blue contour Fig. 2c	MSLP spatial average; contour corr. = 0.25
ME-ridge	Middle East ridge	Blue contour Fig. 2g	Z200 spatial average; contour corr. = 0.14
NAtl-wave	North Atlantic wave	33–60° N, 75°W–25° E	Spatial corr. between pattern and Z200 field
NAm-wave	North American wave	33–60° N, 145–45° W	Spatial corr. between pattern and Z200 field
ISM-OLR	Indian summer monsoon OLR	Blue contour Fig. 2q	OLR spatial average; contour corr. = 0.125
T500-ISM	Indian summer monsoon T500	Blue contour Fig S3g	Z500 spatial average; contour corr. = 0.275
MJO2	OLR MJO index (OMI) pc2, provided by NOAA (https://www.esrl.noaa.gov/psd/mjo/mjoindex/)		
EMed-W500	Eastern Mediterranean subsidence	Blue contour Fig. S3c	W500 spatial average; contour corr. = 0.25
WMed-MSLP	Western Mediterranean high	Blue contour Fig. 2c	MSLP spatial average; contour corr. = 0.25

Each potential precursor identified in Figs. 2 and S3 is shown together with its full name, region of definition and method used to obtain the corresponding index

of action over the eastern US and eastern North Atlantic and a positive centre of action over the western North Atlantic (Fig. 2k). While the spatial position of the wave does not change much over time, its troughs and ridges gradually intensify towards the east when going from lag − 2 towards lag + 2. By construction, the NAtl-wave reaches the maximum intensity over Europe at lag 0 (Fig. 2m) before fading toward the east after reaching Southeast Asia (Fig. 2o). Note that here lag 0 refers to the NAtl-wave index, and not the Etesians index. Thus, as indicated by the upward vertical shift of Fig. 2k–o, lag 0 for the NAtl-wave, corresponds to lag − 1 for the Etesians index (as the NAtl-wave is defined based on the correlation between the Etesians index and the Z200 field at lag − 1). The wave over North America identified at lag − 1 is used to build a precursor time series (NAm-wave, Table 1) of the NAtl-wave.

Similarly, correlation maps between the ME-ridge and the OLR field are calculated and shown in Fig. 2p–t (note that here lag 0 corresponds to lag − 1 in Fig. 2b, g). Positive correlation coefficients are found in correspondence to the ME-ridge at lag − 2 through lag + 2. However, the region of positive correlation, corresponding to enhanced outgoing long wave radiation and clear skies, shifts westwards with increasing lags from the Caspian Sea region to the eastern Mediterranean/North Africa. The westward shift of positive OLR anomalies may be related to the westward propagation of equatorially trapped Rossby waves, as discussed in Rodwell and Hoskins (1996). Negative correlation coefficients are found over central India and the Arabian Sea (Fig. 2q) in correspondence with enhanced convective activity over this area (enhanced convective activity is shown as negative OLR anomalies, following colder than the surroundings convective cloud tops). Enhanced convective activity over this area is considered as a further potential precursor of the ME-ridge and the related time series is calculated as the average of the OLR field over the ISM-OLR region (blue contour in Fig. 2q, Table 1).

Similarly, lagged correlation maps between the temperature at 500 hPa (T500) and the ME-ridge are calculated (Fig. S3 in the Supplementary Material). Enhanced warming is found in correspondence with enhanced convective activity over central India at lags − 2 through lag 0 (Fig. S3f–h). The warming over South Asia shifts westwards following the Rossby wave structures and results in an enhancement of the east–west temperature gradient over the eastern Mediterranean. T500 over central India at lag − 1 (Fig. S3g) is averaged and form a further potential precursor to the ME-ridge (ISM-T500, Table 1).

Correlation maps between the Etesians and MSLP and Z200 fields are calculated also at weekly time scale (Fig. S4 in the Supplementary Material). The correlation maps between the weekly Etesians and the MSLP and Z200 field for lag − 2 to + 2 are shown in Fig. S4a–e and Fig. S4f–j respectively. Similar patterns to those shown in Fig. 2 are detected, however, the significance of the correlation vanishes beyond lags ± 1. The Pers-trough, the NAtl-wave and the ME-ridge time series for the weekly time scale are defined in the same way as for the 3-day time scale. Similarly, calculating the evolution of the correlation maps between the NAtl-wave and ME-ridge and the Z200 and OLR fields respectively, time series for the NAm-wave and the ISM-OLR at weekly time scale are identified in Z200 and OLR fields (Fig. S4l, q in the Supplementary Material). Lagged correlation maps between T500 fields and the ME-ridge for the weekly time scale are shown in Fig. S5 in the Supplementary Material and the ISM-T500 time series is defined at weekly time scale as well. Thus, qualitatively, the same set of potential precursors is identified at weekly time scale, though with some differences in the exact shape and strength of the identified spatial correlation contours.

Overall, the patterns shown in Figs. 2 and S4 suggest that the Etesians may be influenced by three types of precursors: (i) surface local features, i.e. the east–west pressure gradient which may arise due to local diabatic heating of the land surface over the Arabian Peninsula and is here represented by the Persian trough time series; (ii) a mid-latitude wave train originating over the North Atlantic and propagating downstream following the westerly jet (NAtl-wave); (iii) the influence of the ISM (ISM-OLR) via the ridge over the Middle East (ME-ridge).

3.2 Causal effect networks at different time scales

Causal effect networks (CENs) are calculated using the set of five potential precursors of the Etesians identified in Figs. 2 and S4 for the 3-day and 7-day time scales (see Sect. 2 for a thorough definition of the causal discovery tool). The 3-day CEN analysis shows two causal pathways connecting the Etesians with its causal parents: (i) a mid-latitude pathway linking mid-latitude wave activity to the Etesians and (ii) a tropical pathway, linking tropical convective activity to the Etesians via the Middle East high (Fig. 3a). The mid-latitude causal pathway starts from the NAm-wave (lag − 1), which show a positive causal effect on the NAtl-wave (β-value = 0.31) at lag 0. In turn, the NAtl-wave (lag − 1) has a positive effect (β-value = 0.13) on the Etesians at lag 0. Thus, the effect of tropospheric wave activity originating on the North American continent reaches the eastern Mediterranean after two time steps, i.e. 6 days. This is consistent with previous works showing that Rossby wave propagation from the North Atlantic controls the onset of outbreaks of Etesians (Tyrlis et al. 2013).

The tropical causal pathway sees influence of the ISM convective activity on the Etesians being mediated by the ME-ridge (lag − 1), which exhibits a positive causal effect (β-value = 0.24) on the Etesians at lag 0 (Fig. 3a). The

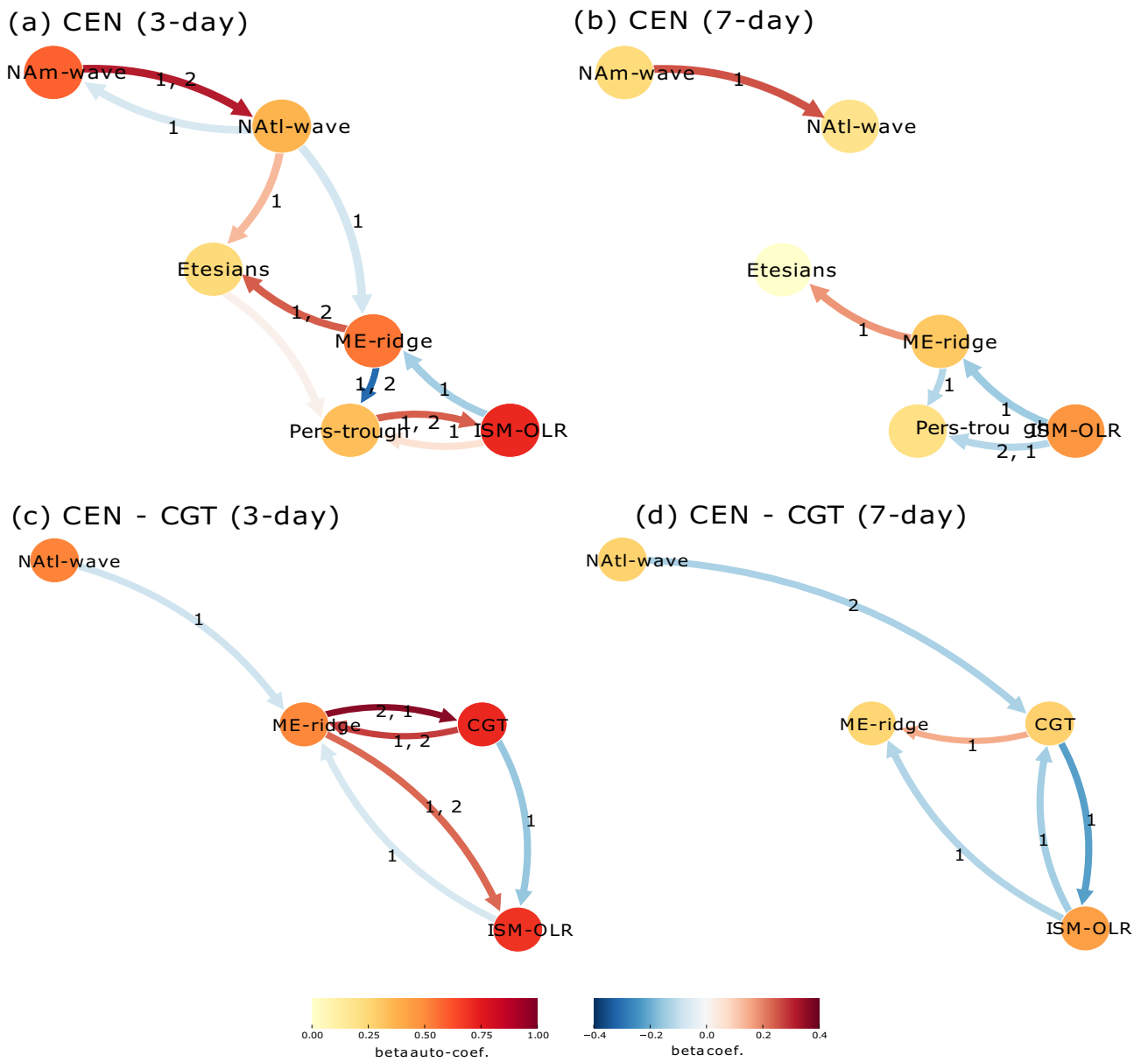

Fig. 3 Causal precursors of the Etesians at different time scales. Panel **a** shows the CEN with six actors: NAtl-wave index, NAm-wave index, the Etesians, ME-ridge, ISM-OLR and Pers.Trough at 3-day time scale. Panel **b**: same as for panel **a** but for the weekly time scale. Panel **c** shows the CEN with four actors: NAtl-wave index, ME-ridge, ISM-OLR and the CGT index at 3-day time scale. Panel **d**: same as for panel **c** but for the weekly time scale Circles (nodes) of each network represent the actors, and the edges of the arrows represent the direction of causality. The colour of the edges (nodes) represents the strength of the causal link, i.e. the β coefficient (auto-β coefficient)

ME-ridge (lag 0) is influenced by the OLR activity over the ISM area (β-value = -0.13) at lag − 1, meaning that enhanced convection over the India peninsula (negative OLR anomalies) is followed by increased Z200 in the ME-ridge. Despite the fact that both the ME-ridge and the NAtl-wave have a positive direct effect on the Etesians, a stronger NAtl-wave (lag − 1) has a negative direct effect on the ME-ridge (β-value = -0.07) at lag 0. Thus, while both positive NAtl-wave and ME-ridge anomalies contribute to positive Etesians anomalies, a stronger NAtl-wave has the effect of weakening the ME-ridge, due to the fact that while propagating eastward, the NAtl-wave causes negative Z200 anomalies over the Middle East region (Fig. 2n). This could be seen as a damping mechanism in the Etesians circulation system. Other local factors, here represented by the Persian trough, appear to be influenced by the ME-ridge and the ISM-OLR at lag − 1 but do not show an outgoing link towards the Etesians. This is in agreement with what is

shown in Fig. 2b, c, where a negative correlation between the Etesians and the Persian through is depicted at lag 0 (Fig. 2c) but not a lag − 1 (Fig. 2b).

Next, we calculate the same CEN for the weekly time scale and show that despite both causal pathways are still present, the effect of the NAtl-wave on both the Etesians and the ME-ridge vanishes at weekly time scales (Fig. 3b). The only remaining direct causal drivers of the Etesians is the ME-ridge (β-value = 0.18), which in turn is influenced by the ISM-OLR (β-value = − 0.15). Thus, while the effect of the mid-latitude wave activity acts on shorter time scales and disappears when weekly averages are analysed, the influence of the ISM acts on longer time scales and is consistent in sign and strength both at 3- and 7-day time scales (see Sect. 4 for further insight). To compare causal effect values with a standard measure, we also calculate the amount of variability explained by the four main causal links, i.e. NAtl-wave → Etesians, NAm-wave → NAtl-wave, ME-ridge → Etesians and ISM-OLR → ME-ridge. The total variance explained (calculated as the square value of the r-value) is reported in Table S1 in the Supplementary Material. Values range from $r^2 \sim 0.20$ for the NAm-wave → NAtl-wave to $r^2 \sim 0.05$ for the ME-ridge → Etesians.

The CENs in Fig. 3 show that, both at 3- and 7-day time scale, the Persian trough index is not a causal precursor of the Etesians but rather a feature appearing contemporaneously to the latter. Moreover, these CENs suggest that the ME-ridge arises as a result of the heat source provided by the ISM rather than local surface diabatic heating over the Arabian Peninsula. To check this hypothesis, we build a CEN with the Etesians, ISM-OLR, ME-ridge and ISM-T500, showing that enhanced convective activity over India causes warming in the middle of the troposphere, which in turn propagates westwards causing a strengthening of the ME-ridge (Fig. S6 in the Supplementary Material). This evolution is consistent with the westward propagation of a Rossby wave. Again, this causal pathway is shown both for 3- and 7-day time scales (Fig. S6a and S6b respectively, see Text S2 in the Supplementary Material for further details). Moreover, we check whether the CENs shown in Fig. 3a, b are stable when perturbed by adding further actors to the network. We add three further actors: (i) the western Mediterranean region of positive correlation between MSLP and the Etesians (WMed-MSLP, Fig. 2c), (ii) the Madden and Julian outgoing longwave radiation index second principal component (MJO2) and (iii) the region of positive correlation between the Etesians and subsidence (EMed-W500, Fig. S3c). The resulting CENs (3-day and weekly time scale, Fig. S6c and S6d respectively) show consistent causal links to those shown in Fig. 3a, b, with the addition of the following links: the WMed-MSLP has only one positive causal link on the Pers-though, meaning that when the WMed-MSLP intensifies, the Pers-though will weaken in the following week. This highlights the fact that the WMed-MSLP and the Pers-though peak in the same moment. WMed-MSLP does not show any incoming link, so it seems to be disconnected from both the mid-latitude and the tropical – ISM pathways. MJO2 (see Table 1 for further details) shows a positive influence on the ISM-OLR index at weekly time scale (Fig. S6d), while no influence is detected at 3-day time scale (Fig. S6c). This results is in agreement with what shown in Di Capua et al. (2020a), where at weekly time scale, MJO2 had a similar link towards the monsoon trough rainfall. At shorter (3-day) time scale, the lack of links may be explained by the fact that the MJO (which has a typical time scale of 30 to 90 days) acts on a longer time scale and its effect is therefore not strong enough at 3-day time scale. For subsidence, i.e. EMed-W500, three incoming positive causal links are detected from the NAtl-wave, the ME-ridge and the Etesians. In turn, EMed-W500 shows a negative causal link toward Pers-through. Thus, although from a dynamical point of view, the Etesians are certainly related to subsidence (as shown in Fig. S3c), this relationship has a contemporaneous nature, hence the signal does not show up when lag − 1 (or longer) is analysed.

One important mid-latitude driver of the ISM activity is represented by the CGT pattern. Here, we study the connection between the CGT index (Z200 averaged over the region 35°–40° N, 60°–70° E, see blue box in Fig. S7 in the Supplementary Material) and the ME-ridge–ISM-OLR–NAtl-wave causal network. CENs built using these four indices show a close link between the ME-ridge and the CGT index (Fig. 3c, d). In the 3-day CEN, a strong positive feedback is present between the ME-ridge and the CGT index, showing that a stronger CGT index (lag − 1) is followed by a stronger ME-ridge at lag 0 (β-value = 0.28), and a stronger ME-ridge (lag − 2) is followed by a stronger CGT at lag 0 (β-value = 0.36) (Fig. 3c). This is also shown in Fig. S7c–e, where the positive anomaly propagates from the CGT region at lag 0 towards the Middle East and eastern North Africa at lag + 2. This signal propagation is consistent with a Rossby wave propagating from the ISM towards North Africa, i.e. the monsoon–desert mechanism, and it has been described in details in Di Capua et al. (2020a, b). Causal links from the ISM-OLR and the NAtl-wave towards the ME-ridge are consistent with what shown in Fig. 3a. A negative link from the CGT towards the ISM-OLR index (β-value = − 0.16) depicts the effect of the mid-latitudes on the ISM system, as described in Di Capua et al. (2020a). Analysing the same CEN at weekly time scales (Fig. 3d) shows similar causal links with three main differences: (i) the two-way effect between the CGT index and the ISM-OLR (expected from previous work, see Di Capua et al. 2020a, b) is now clearly visible as a positive feedback between these two variables, (ii) the negative effect of the NAtl-wave is not directed towards the ME-ridge but toward

the CGT index (and thus still affects the ME-ridge though indirectly) and (iii) the ME-ridge only shows incoming links, strengthening the hypothesis that the effect of tropical drivers becomes more relevant when the length of the time step increases. Note that, although both causal links between the CGT and the ISM-OLR index are negative, this still constitutes a positive feedback: when the CGT increases, the ISM-OLR index decreases (corresponding to enhanced rainfall), while when ISM-OLR decreases, it is followed by an increase in the CGT. Thus, the initial increase in the CGT index is reinforced by the interaction with ISM-OLR.

While the ISM rainfall season peaks in July–August, the Etesians variability diminished in the middle part of the summer (though this corresponds to more stable northerlies). Thus, to assess the dependence of the results shown in Figs. 2 and 3 on the exact choice of summer months, we produce the same analysis for the following three pairs of months: June-July (JJ), July–August (JA) and August–September (AS). Similarly to what shown in Fig. 2, potential precursors at 3-day time scale are now calculated for the JJ, JA and AS periods and the resulting spatial patterns are shown in Fig. 4a–d (JJ), Fig. 4e–h (JA) and Fig. 4i–l (AS). Qualitatively, the same regions can be identified, although the strength of the correlation diminished in August–September. This change is most noticeable for the ME-ridge (Fig. 4j) and the ISM-OLR region (Fig. 4l), both regions shrinking in size, while their correlation values are weaker compared to those shown for JJ (Fig. 4b, d) and JA (Fig. 4f, h). Next, for each sub-period, we calculate a CEN with the same set of actors as shown in Fig. 3a, i.e. NAm-wave, NAtl-wave, Etesians, ME-ridge, ISM-OLR and Pers-through (not shown). Moreover, for each sub-period, we produce a 1000 CEN, each obtained by removing 11 years, and we plot the resulting β value distributions for the two most relevant causal pathways, i.e., the mid-latitude (NAm-wave → NAtl-wave → Etesians) and the tropical (ISM-OLR → ME-ridge → Etesians) pathway (Fig. 4m). For each of the four causal links, and for each sub-period, the corresponding spread in β-values is represented by the boxplot. To compare the JJ, JA and AS β-values with the corresponding JJAS β-values, the CEN shown in Fig. 3a is also re-calculated a 1000 times (each time randomly removing 11 years) and the corresponding spread is shown in Fig. 4m by horizontal shading, showing for each link the mean β-values and the 95% confidence interval. Despite some quantitative differences, in general, the distribution of β-values for different sub-periods overlaps with the JJAS range (Fig. 4m). For the NAm-wave → NAtl-wave link, AS β-values closely follow the JJAS distribution (mean β-value ~ 0.31), while JJ and JA β-values show a tendency towards higher values (mean β-value ~ 0.35). Similarly, for the NAtl-wave → Etesians link, AS β-values again follow the JJAS β-value closely (mean β-value ~ 0.12), while JJ β-values are somewhat stronger (mean β-value ~ 0.16) and JA β-values are somewhat weaker (mean β-value ~ 0.1). For the ISM-OLR → Etesians link, there is a general tendency to slightly lower (absolute) β-values for all subperiods (JJ and JA mean β-value ~ − 0.1 compared to JJAS mean β-value ~ − 0.13). The AS β-value distribution (mean β-value ~ − 0.05) is the only case where the JJAS and the AS β-values distribution do not overlap. For the ME-ridge → Etesians link, the JJ β-values distribution follows closely JJAS (mean β-value ~ 0.24), while the JA and AS mean β-values are somewhat weaker (mean β-value ~ 0.20 and β-value ~ 0.18 respectively). In general, the influence of both the ISM–Etesians and the NAtl-wave – Etesians pathways is stronger in the early part of the season JJ, and weakens towards AS. However, the sign and the direction of the causal links always match those of the JJAS CEN. The same analysis is also performed for the weekly time scale with qualitatively similar results (Fig. S8 in the Supplementary Material). Thus, for the next steps of this analysis, we will keep using the JJAS season.

We check the stationarity of the most important identified causal links over the analysed period by calculating each CEN on an 9-year moving window and then calculating the trend on the time series of the 36 β-values obtained (one β-value for each 9-year moving window, thus 36 time steps obtained from the original 44-year long time series, Fig. S9 in the Supplementary Material). Results show that the sign of the causal links remains stable even when only 9 years on a moving window are considered (Fig. S9). One exception is the link NAtl-wave$_{t=-1}$ → Etesians$_{t=0}$|all, which shows a downward linear trend in its β-value of − 0.0025/year, thus a total decrease over 36 years of 0.09, which corresponds to a ~ 50% decrease with respect to the 44-year value of β-value ~ − 0.13 shown in Fig. 3a. While the effect of the NAtl-wave on the Etesians shows a negative trend over the analysed period (p-value = 0.12, Fig. S9a in the Supplementary Material), we do not detect any significant trend in the involved actors themselves. Since the NAtl-wave index is obtained by calculating the spatial correlation between the pattern shown in the blue box in Fig. 2g and the Z200 field over the same area for each time step (as explained in Sect. 3.1), the fact that the NAtl-wave index does not show a significant trend may still hide changes inside the analysed pattern. To investigate this hypothesis, we plot composite of Z200 anomalies over days with NAtl-wave > 1 s.d. for the first and last 15 years of the 1979–2022 period (1979–1993 and 2008–2022 respectively). Comparing the spatial patterns shown in Fig. S10a, b (see Supplementary Material), the same wave (NAtl-wave), as described earlier, appears. However, the intensity of the ridges over the eastern Canada and central-eastern Europe declines by about 14 m. Calculating the difference (late period minus early period) further quantifies these differences, (Fig. S10c in the Supplementary Material).

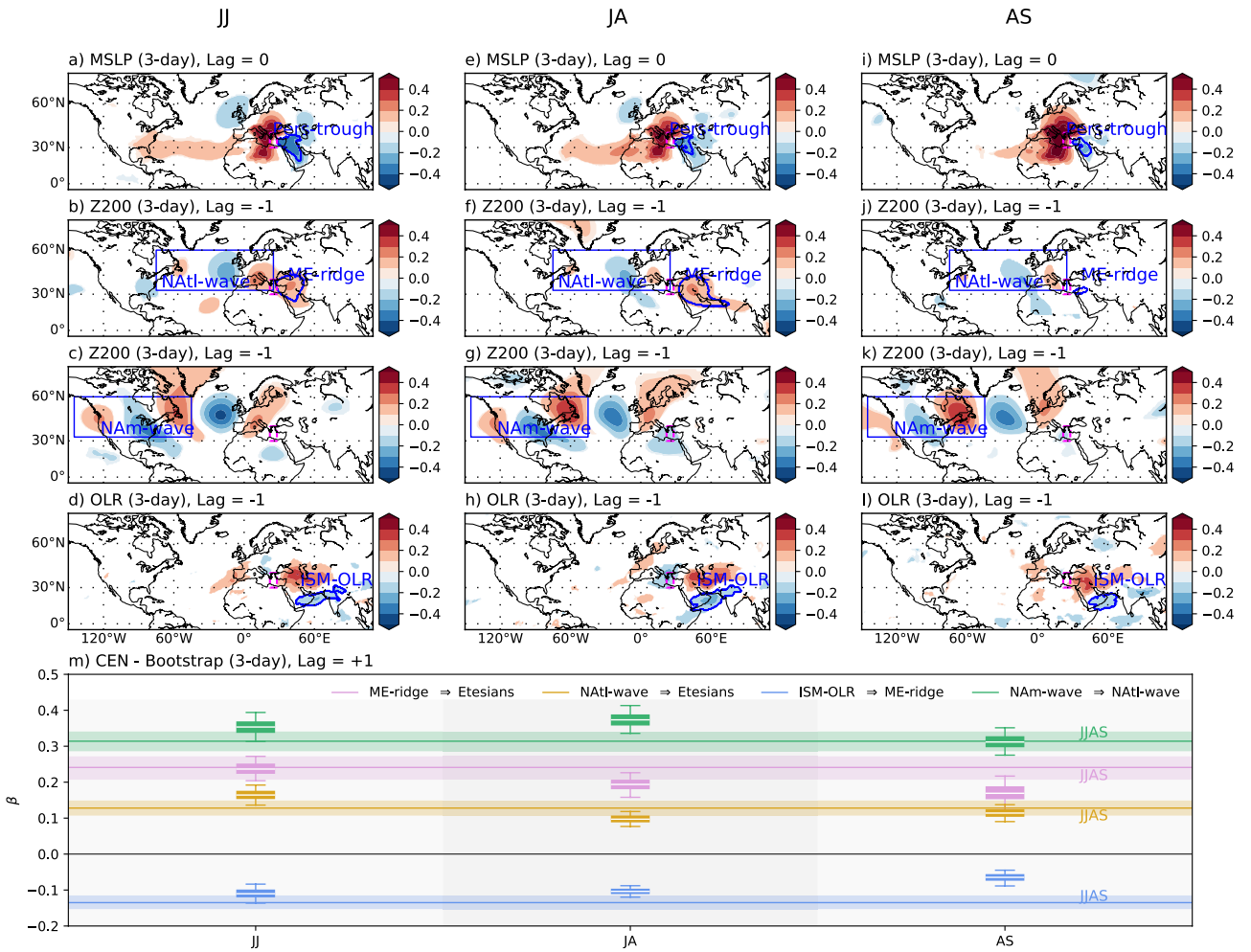

Fig. 4 Causal precursors of the Etesians for different JJAS sub-periods. Panel **a** shows the correlation map between the Etesians index time series and the MSLP field at lag 0 (3-day time steps) for the JJ period. Panel **b** shows the correlation map between the Etesians index time series and the Z200 field at lag − 1 for the JJ period. Panel **c** shows the correlation map between the NAtl-wave index and the Z200 field at lag − 1 for the JJ period. Panel **d** shows the correlation map between the ME-ridge index and the OLR field at lag -1 for the JJ period. Panels **e**–**h** and **i**–**l** same as for panels **a**–**d** but for JA and AS period respectively. Grid points for which the correlation is not significant at $\alpha < 0.05$ (after applying the Benjamini–Hochberg correction) are shown in white. Panel **m** shows the box plots for the 1000 β values calculated for the links NAtl-wave → Etesians, NAm-wave → NAtl-wave, ME-ridge → Etesians and ISM-OLR → ME-ridge and for the three analysed JJAS sub-periods, i.e. JJ, JA and AS. The shaded horizontal lined represent the JJAS 1000 β values calculated for the JJAS period. The whiskers of each box plot, and the shaded horizontal lines, represent the 95% confidence interval. The bootstrap is calculated by removing 11 years for the JJAS sub-period and 11 years for the full JJAS season

Hence, although the overall NAtl-wave index does not change significantly, the intensity of the ridge right to the west of the Etesians region declines. This decline may then explain the negative trend in the NAtl-wave → Etesians β-values shown in Fig. S9a (in the Supplementary Material).

3.3 Causal maps of mid-latitude and tropical drivers

The causal effect of both mid-latitude and tropical drivers on the eastern Mediterranean circulation is further analysed also in its spatial structure. We calculate causal maps (see Sect. 2 for a detailed description) which are similar in concept to correlation maps, but instead of the correlation coefficient, each gridpoint shows the β-value calculated by the CEN build with three (fixed) tropical – mid-latitude drivers (NAtl-wave, ME-ridge and ISM-OLR) and a fourth actor, which is the gridpoint time series of a selected field. For example, Fig. 5 shows causal maps for the effect NAtl-wave (and excluding the effect of the other two causal drivers and the field itself) on several other atmospheric fields both on the 2D horizontal plane and in the vertical section and for both 3- and 7-day time scales (left and right column respectively).

The causal effect of the NAtl-wave (lag − 1) on the MSLP field at lag 0 (NAtl-wave$_{t=-1}$ → MSLP$_{t=0}$|all) is shown in Fig. 5a: the signature of the mid-latitude wave train is visible in the North Atlantic/European sectors, with negative β-values over the British Isles and central Asia, and positive β-values over eastern Europe and western China. Positive anomalies are also shown west of the Gibraltar Strait, extending to eastern North Africa. A weak negative signature is also present over the eastern Mediterranean. The causal map for the effect of the NAtl-wave (lag − 1) on the Z200 field at lag 0 (Fig. 5c) shows a clear mid-latitude wave signature with positive and negative β-values partly corresponding to the centres of actions shown in Fig. 5a. Thus, this map shows the propagation of the wave signal toward the east. The effect of the NAtl-wave (lag − 1) on the V850 field at lag 0 (Fig. 5e) shows a clear wave signature highlighting the regions of enhanced southerlies over central Europe and central Asia and northerlies over western Russia, extending via the Black Sea towards the eastern Mediterranean and Libya. Weekly causal maps for the same fields are shown in Fig. 5b, d, f displaying a still present, but less prominent, wave-like structure and weak northerlies only at the top left corner of the Etesians box (Fig. 5f).

The causal effect is also studied in the vertical section in Fig. 5g–j, showing the causal effect of NAtl-wave on the vertical (W-wind) and meridional (V-wind) wind fields averaged over the 32–40° N latitudinal belt between 0° and 110°E. The causal effect of the NAtl-wave on the W-wind shows evidence of ascending motions (negative β-values ~ 0.2–0.3) between 40°–60° E extending from the middle of the troposphere to the 200 hPa pressure level. Ascending motions are also present over the eastern Mediterranean but confined between 200 and 100 hPa pressure levels (Fig. 5g). Descending motions (positive β-values) are shown on the western Tibetan Plateau (60°–90° E) and in the lower levels over the eastern Mediterranean, though the latter are very weak (Fig. 5g). The causal map showing the effect of the NAtl-wave on the V-wind field depicts a very clear almost-barotropic wave-like structure throughout the entire troposphere, with southerlies over the western Mediterranean and the Middle East region and northerlies over the eastern Mediterranean region and the Tibetan Plateau (Fig. 5i). Weekly vertical causal maps also show very few significant gridpoints, though weak northerlies are still shown in Fig. 5j on the eastern Mediterranean.

The effect of the NAtl-wave on the circulation in the Mediterranean region shows a wave response, which can be seen both in the 2D horizontal causal maps and the vertical levels. This wave-like response shows the typical characteristics of a quasi-barotropic mid-latitude eastward propagating Rossby wave, with a sequence of high and low pressure centres accompanied by northerly and southerly winds which span from the lower to the upper troposphere.

Next, we analyse the causal effect of the ME-ridge on MSLP and V850 horizonal fields for both 3- and 7-day time scales (Fig. 6). The causal map for the link ME-ridge$_{t=-1}$ → MSLP$_{t=0}$|all (Fig. 6a) shows a clear east–west MSLP gradient with positive anomalies (positive β-values) over Italy and Libya (β-value ~ 0.1–0.2) and negative anomalies over the Persian trough region (β-value ~ 0.2–0.4). Thus, the ME-ridge is responsible for the formation of the typical east–west MSLP gradient at 3-day time scales, which is conducive for Etesians winds (Fig. 1b) and is also partly reflected in the seasonal climatology of the region (Fig. S1c). This response is markedly visible as an effect of the ME-ridge (Fig. 6a), while it was much weaker and not clearly identifiable as a response of the NAtl-wave (Fig. 5a). The causal map for the link ME-ridge$_{t=-1}$ → V850$_{t=0}$|all (Fig. 6c) shows negative β-value ~ 0.1–0.3 corresponding to northerlies over the eastern Mediterranean, i.e. enhanced Etesians follow a stronger ME-ridge with a 3-day time step delay. These northerlies, i.e. the Etesians, form as a response to the west–east MSLP gradient displayed in Fig. 6a. Northerlies are also present at the Himalayan foothills and the offshore regions of the western Ghats. Southerlies are shown over the south-eastern tip of the Arabian Peninsula and Southeast Asia. Weekly causal maps exhibit a similar east–west MSLP gradient (Fig. 6b) though with reduced causal link strength (β-value ~ 0.1–0.2) and a weaker but still clearly visible northerly signature over the eastern Mediterranean (β-value ~ 0.2–0.3, Fig. 6d).

Causal maps of vertical cross-sections for the causal link ME-ridge$_{t=-1}$ → W-wind$_{t=0}$|all at 3-day time scale (Fig. 6e) show enhanced subsidence (positive β-values ~ 0.2–0.3) between 20° and 30°E, corresponding to the eastern Mediterranean. Northerlies over the eastern Mediterranean can be dynamically explained as a response to the warming at mid- and high-tropospheric levels in the vicinity of the ME-ridge. Isentropic surfaces bend down in the region of diabatic warming resulting in sloping isentropic surfaces over the eastern Mediterranean. In the absence of diabatic processes, the northerlies over the eastern Mediterranean will generally follow the isentropic surfaces and acquire a significant downward component that explains the observed subsidence over the region. Ascending motions (negative β-values ~ -0.2–0.3) are located over the Middle East and the Tibetan Plateau. Vertical causal maps for the causal link ME-ridge$_{t=-1}$ → V-wind$_{t=0}$|all at 3-day time scale (Fig. 6g) show northerlies located over the eastern Mediterranean (negative β-values ~ -0.2–0.3) but confined in the lower troposphere between 900 and 500 hPa. In the upper troposphere, southerlies are located over the western Mediterranean, and the Tibetan Plateau, while northerlies are located over the Middle East. Note that the southerly-northerly pair

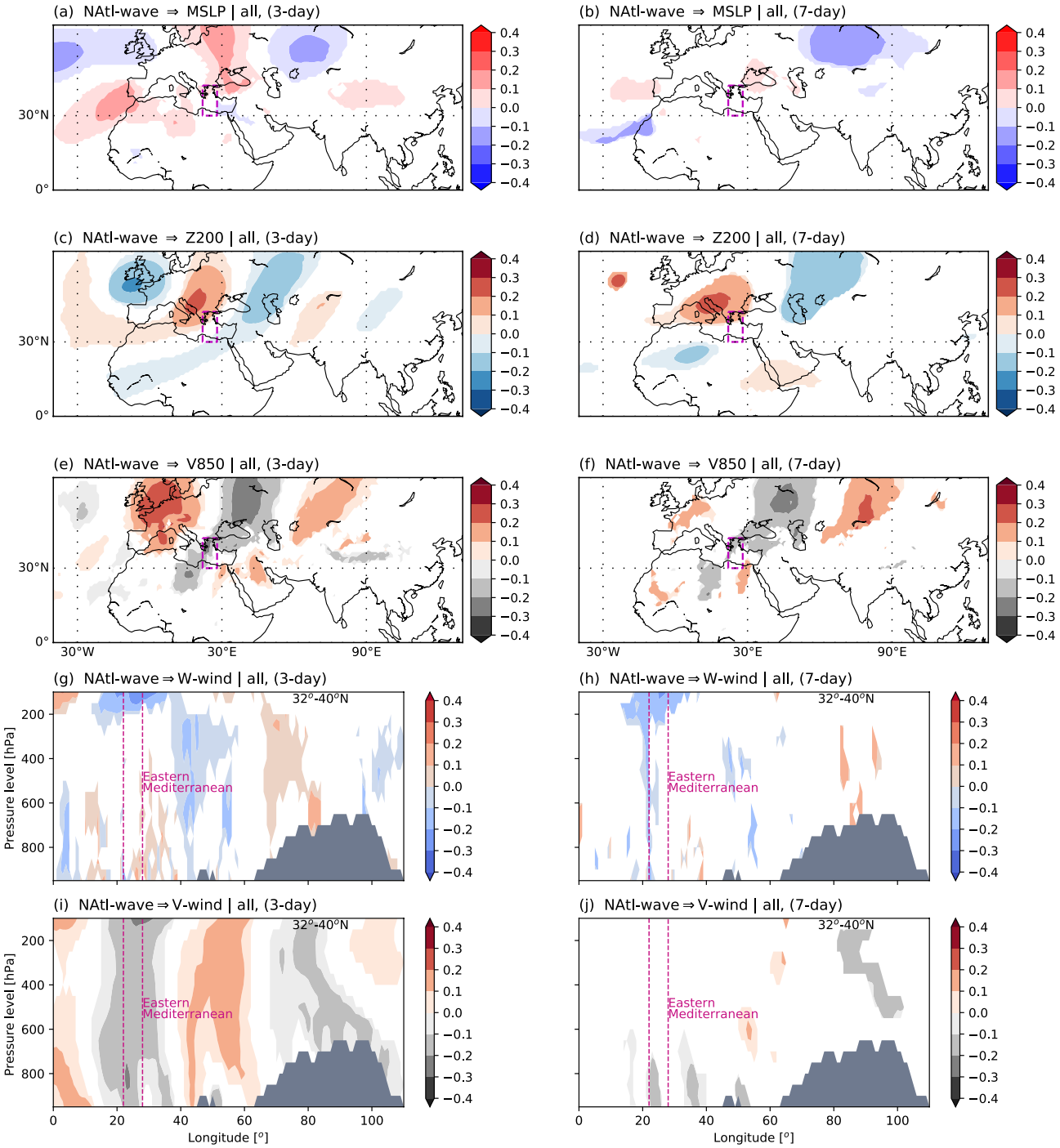

Fig. 5 Causal effect of the NAtl-wave. Panel **a**: horizontal causal map for the link NAtl-wave$_{t\ =\ -1}$→MSLP$_{t=0}$|all, where NAtl-wave$_{t\ =\ -1}$→MSLP$_{t=0}$|all represents the causal effect of the NAtl-wave on MSLP where the NAtl-wave leads the MSLP field by one time step. Panel **b**: same as for panel **a** but for weekly time scale. Panel c: horizontal causal map for the link NAtl-wave$_{t\ =\ -1}$→Z200$_{t=0}$|all. Panel **d**: same as for panel **c** but for weekly time scale. Panel **e**: horizontal causal map for the link NAtl-wave$_{t\ =\ -1}$→V850$_{t=0}$|all. Panel **f**: same as for panel **e** but for weekly time scale. Panel **g**: vertical causal map for the link NAtl-wave$_{t\ =\ -1}$→W-wind$_{t=0}$|all. Panel **h**: same as for panel **g** but for weekly time scale. Panel **i**: vertical causal map for the link NAtl-wave$_{t\ =\ -1}$→V-wind$_{t=0}$|all. Panel **j**: same as for panel **i** but for weekly time scale. For W-wind, red shading represents subsidence, while blue shading represent ascent. For V-wind, red shading represents southerlies, while gray shading represent northerlies

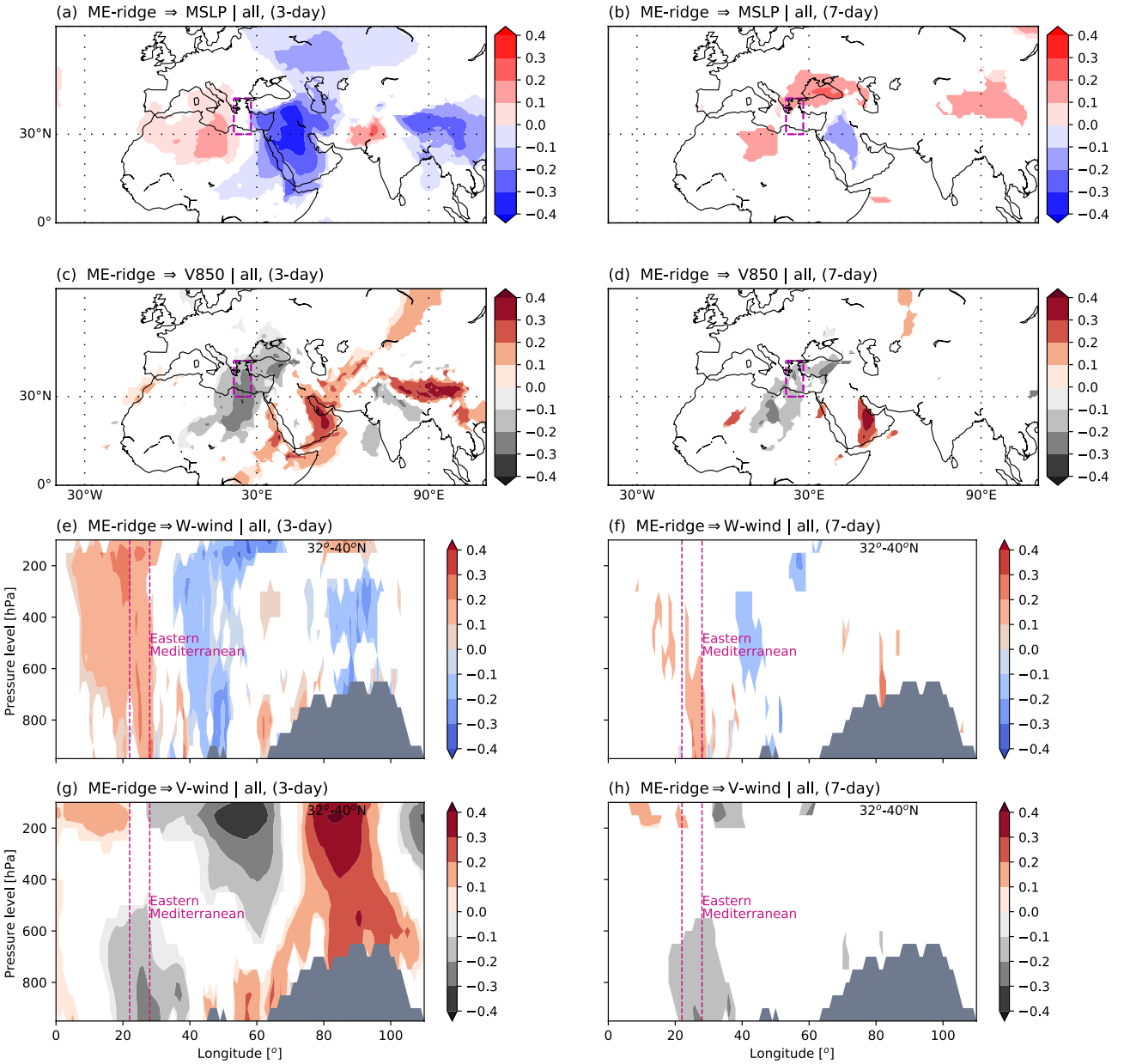

Fig. 6 Causal effect of the ME-ridge. Panel **a**: horizontal causal map for the link ME-ridge$_{t=-1}$→MSLP$_{t=0}$|all, where ME-ridge$_{t=-1}$→MSLP$_{t=0}$|all represents the causal effect of the ME-ridge on MSLP where the ME-ridge leads the MSLP field by one time step. Panel **b**: same as for panel **a** but for weekly time scale. Panel **c**: horizontal causal map for the link ME-ridge$_{t=-1}$→Z200$_{t=0}$|all. Panel **d**: same as for panel **c** but for weekly time scale. Panel **e**: vertical causal map for the link ME-ridge$_{t=-1}$→W-wind$_{t=0}$|all. Panel **f**: same as for panel **e** but for weekly time scale. Panel **g**: vertical causal map for the link ME-ridge$_{t=-1}$→V-wind$_{t=0}$|all. Panel **h**: same as for panel **g** but for weekly time scale. For W-wind, red shading represents subsidence, while blue shading represent ascent. For V-wind, red shading represents southerlies, while gray shading represent northerlies

located between the western Mediterranean and the Middle East corresponds to the upper level anticyclone which is shifting from the Middle East towards Northern Africa and the western Mediterranean (see also Figs. S11i and S11j in the Supplementary Material). Causal maps on vertical cross-sections created with 7-day averaged fields show weaker but still clearly recognizable descending motions (Fig. 6f) and northerlies (Fig. 6h) located over the eastern Mediterranean.

Thus, the ME-ridge shows a greater causal effect over the Mediterranean (in terms of area affected and strength of the β-values) than the NAtl-wave and the effect of the ME-ridge on subsidence is stronger and more marked than that of the NAtl-wave. Moreover, the response to the ME-ridge shows

characteristics which hint to its tropical nature: while the vertical structure of the NAtl-wave response is quasi-barotropic, the response to the ME-ridge shows features that change with height. This behaviour is also found in a tropical heat low, showing a convergence and cyclonic circulation at the lower level, and divergence and anticyclonic circulation at the upper level.

Finally, we analyse the causal effect of ISM-OLR on T500 and Z200 horizonal fields for both 3- and 7-day time scales (Fig. 7). The causal map for the link ISM-$OLR_{t=-1} \rightarrow T500_{t=0}|all$ shows warming in the middle troposphere over the Arabian Sea, Iran and the Arabian Peninsula (Fig. 7a). The causal map for the link ISM-$OLR_{t=-1} \rightarrow Z200_{t=0}|all$ depicts positive β-values ~ 0.1–0.2 over the Middle East and the eastern Mediterranean, thus showing an intensification of the ME-ridge following enhanced convective activity in the ISM region (Fig. 7c). Positive, though weak, β-values ~ 0.1 extend to the entire North Africa, in agreement with Di Capua et al. (2020b), who identified an influence of the ISM convection on North Africa, also known in the literature as monsoon-desert mechanism. Negative β-values ~ − 0.1–0.2 are shown over Kazakhstan, indicating lower Z200 anomalies following enhanced convective activity over India (Fig. 7c). When the weekly time scale is analysed, the influence of the ISM convection on North Africa and the Middle East increased in term of in affected area and strength of the β-value ~ 0.2–0.3, thus showing that the effect of the ISM has a stronger impact on nearby and remote regions which intensify at longer time scales. This is consistent with studies showing that the effect of tropical convective activity, which can act as a source of Rossby waves, acts on times scales of about two weeks (Branstator 2014). The ISM convective activity provides a heat source via latent heat release which builds up over a period of four months and can be a source of Rossby waves.

Vertical causal maps show the effect of ISM-OLR on both W-wind and Θ fields at lag − 1 for both 3- and 7-day time scales. The causal map for the link ISM-$OLR_{t=-1} \rightarrow W\text{-}wind_{t=0}|all$ shows some descent over the eastern Mediterranean (positive β-values ~ 0.1–0.2) between 300 and 200 hPa (Fig. 7e). Increasing Θ can be linked to diabatic heating originating from latent heat released by convective rainfall over the Indian Peninsula. Dynamically, as explained for the ME-ridge, this is related to diabatic warming of the middle troposphere which bends the isentropes and promotes subsidence. Descent is also shown over North Africa and the Middle East region, while ascending motions (negative β-values ~ 0.1–0.2) are located on the western flank of the Tibetan Plateau throughout the entire tropospheric column (Fig. 7e). The causal map for the link ISM-$OLR_{t=-1} \rightarrow \Theta_{t=0}|all$ shows increased potential temperatures (positive β-values ~ 0.2–0.3) between 500 and 200 hPa over the Middle East region (Fig. 7g). Weekly vertical causal maps show a strengthening of both descending motions over the eastern Mediterranean (β-values ~ 0.2–0.3, Fig. 7f) and diabatic heating over the Middle East (β-values ~ 0.2–0.3, Fig. 7h). Thus, like for the horizonal causal maps, the effect of the ISM convective activity strengthens when longer time steps are analysed.

Finally, we estimated horizontal causal maps of the ISM-OLR convection on MSLP, precipitation and W500 fields. The resulting maps depict enhanced rainfall over central Indian, accompanied by stronger ascending motions and lower MSLP anomalies centred over the Arabian Sea and expanding towards the Persian trough (see Fig. S11a–f in Supplementary Material). Similarly, we estimate vertical causal maps for W-wind and Θ but for the latitudinal band 17°–28° N, corresponding to Central India latitudes, and the results shown enhanced ascending motions over central India (Fig. S11g, h) and enhanced diabatic heating extending from central Indian towards North Africa (Fig. S11i, j).

4 Discussion and conclusions

By applying causal effect networks (CENs), we have identified the causal precursors of mean state of the Etesians during boreal summer (June to September) and have shown that two *causal pathways* can be identified which govern the intraseasonal variability of the Etesians. The first pathway is a mid-latitude causal pathway, where a Rossby wave train originating over North America propagates towards the North Atlantic/European sector and affects the Etesians about a week later. The second pathway is characterized by the propagation of equatorially trapped Rossby waves originating from the Indian monsoon region: enhanced convective activity in the Indian summer monsoon regions (ISM), leading to higher Z200 anomalies over the Middle East (ME-ridge), which in turn drive stronger Etesians on a time scale from one-to-two weeks. The ME-ridge is also found to affect local MSLP anomalies over the Arabian Peninsula, thus hinting to the fact that lower MSLP pressure values are a consequence of subsidence in this region caused by the intensification of the Z200 ridge aloft and not vice versa (Fig. 3a, b). A stronger upper level ridge over the Middle East could enhance subsidence and clear skies over the region resulting to more intense surface heating and intensification of the heat low. In turn, it can tighten the pressure gradient over the eastern Mediterranean and eventually strengthen the Etesians. While the mid-latitude pathway disappears when the weekly time scale (instead of 3-day time scale) is analysed, the ISM–Middle East pathway remains stable. This behaviour highlights the difference in the typical time scales at which mid-latitude circulation and tropical convective activity act: while mid-latitude circulation anomalies are best represented at synoptic time

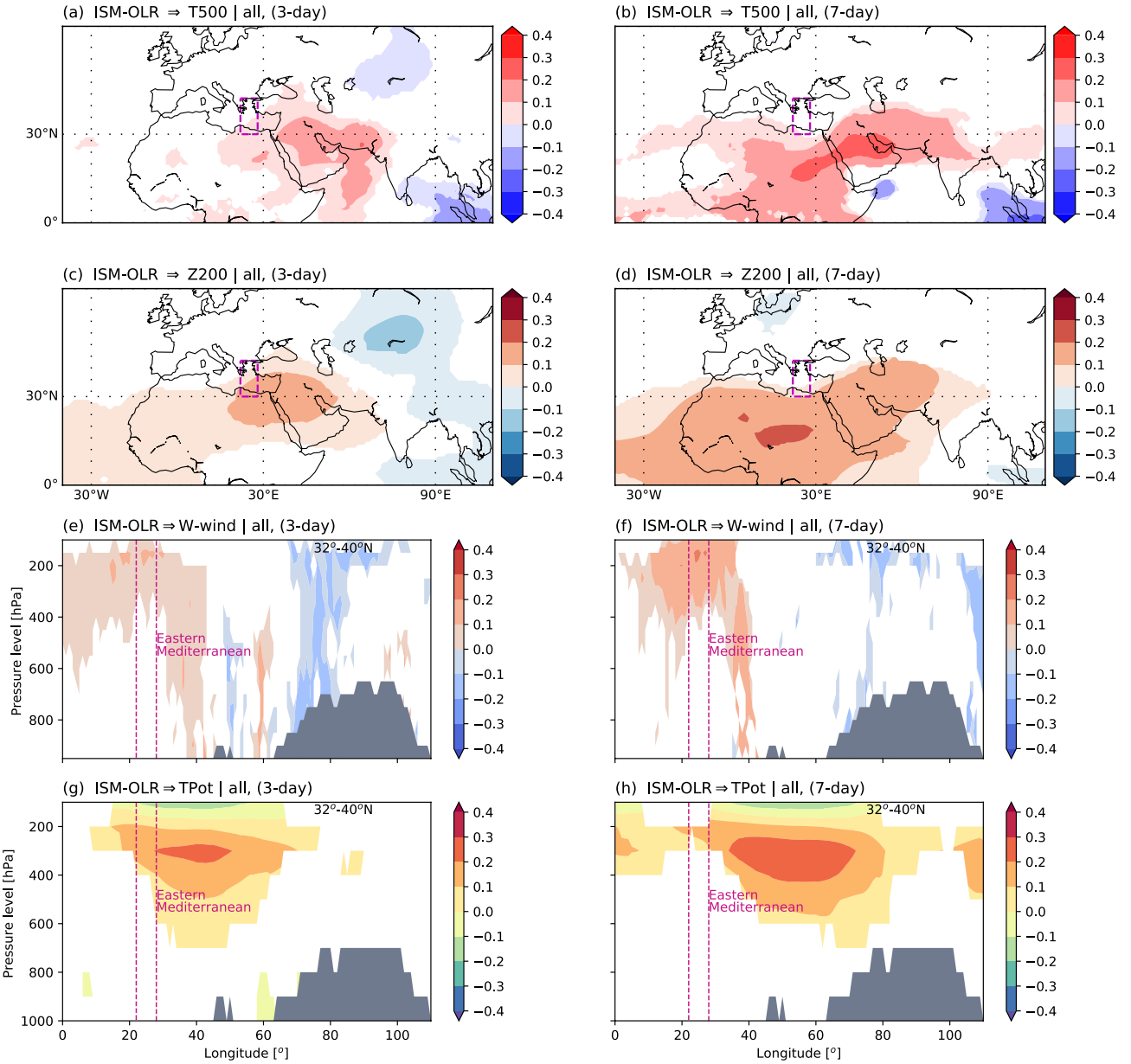

Fig. 7 Causal effect of the ISM-OLR. Panel **a**: horizontal causal map for the link ISM-OLR$_{t\,=\,-1} \rightarrow$T500$_{t=0}$|all, where ISM-OLR$_{t\,=\,-1} \rightarrow$T500$_{t=0}$|all represents the causal effect of the ISM-OLR on T500 where the ISM-OLR leads the T500 field by one time step. Panel **b**: same as for panel **a** but for weekly time scale. Panel **c**: horizontal causal map for the link ISM-OLR$_{t\,=\,-1} \rightarrow$Z200$_{t=0}$|all. Panel **d**: same as for panel **c** but for weekly time scale. Panel **e**: vertical causal map for the link ISM-OLR$_{t\,=\,-1} \rightarrow$W-wind$_{t=0}$|all. Panel **f**: same as for panel **e** but for weekly time scale. Panel **g**: vertical causal map for the link ISM-OLR$_{t\,=\,-1} \rightarrow \Theta_{t=0}$|all. Panel **h**: same as for panel **g** but for weekly time scale. For W-wind, red shading represents subsidence, while blue shading represent ascent

scales, the ISM system acts on sub-monthly time scales (Suhas et al. 2012). The relationship between the Middle East ridge and the circumglobal teleconnection index is also assessed, showing that while at 3-day time scale these two actors are closely related (strong positive feedback, Fig. 3c), at weekly time scale the CGT-index drives the ME-ridge (Fig. 3d). When the stationarity over time of the most important causal links is checked, a 50% decrease in the strength of the β-value of the causal link between the North Atlantic wave activity and the Etesians is detected over the 1979–2022 period (Fig. S9). Finally, it is important to notice that CEN are better suited to study the mean state of the systems, thus the causal pathways presented in the analysed CENs may vary when only extreme states of the Etesians are considered.

Causal maps provide a deeper insight into the spatial patterns of the causal links detected in the CEN analysis. The causal effect of each of the most important causal precursors of the Etesians, i.e. the North Atlantic wave, the Middle East ridge and the ISM convective activity, is now analysed on a 2D field. In general, the patterns shown in Figs. 5–7 agree with those shown in Fig. 3 but add further detail to the general picture. Four key messages are obtained: (i) the mid-latitude wave has a (quasi) barotropic effect on meridional wind velocity and geopotential height fields, which is stronger in the mid-latitude sector and shows only a limited influence on the east–west Mediterranean MSLP gradient which is needed to establish the Etesians; (ii) the Middle East ridges has the strongest role in driving both subsidence and northerlies over the eastern Mediterranean, and it has a clear role in establishing the heat low over the Middle East; (iii) the ISM convection causes warming over the Arabian Sea and Middle East which results in larger geopotential heights anomalies over the Middle East region; (iv) the direct effect of the North Atlantic wave and the Middle East ridge weakens at weekly time scales while that of the ISM intensifies.

Our results shed light on the diverse influence of mid-latitude and tropical drivers on the eastern Mediterranean tropospheric circulation. The ISM not only affects the seasonal background northerlies (Tyrlis et al. 2013), but also affects the intraseasonal variability with a causal strength which is comparable with that of the mid-latitude influence.

The Indian monsoon–Middle East ridge causal pathway can be interpreted in the context of the monsoon–desert mechanism, which connects seasonal ISM convective activity to a Rossby wave response to the west (induced by the heat source provided by deep convection) and subsidence motions centred over eastern North Africa (Rodwell and Hoskins 1996). When the effect of convective activity over the ISM region is analysed on a 2D field (causal maps in Fig. 7), its direct effect on both geopotential height fields and subsidence over the eastern Mediterranean and North Africa shows an evolution over time in both the spatial patterns and the strength of the causal links. At shorter (3-day) time scales, the causal effect of the convection over the ISM region shows its peak over the Middle East and the eastern Mediterranean, with β-values ~ 0.1–0.2 (Fig. 7c). At weekly time scales, the peak of the causal effect has shifted south-westward towards the Sahel region and reaches β-values ~ 0.2–0.3 (Fig. 7d), showing close similarity to that identified by Di Capua et al. (2020b) in their Fig. 3c. Thus, the effect of the ISM convection on the Middle East ridge can be interpreted as a "transient" in the expansion of the effect of the ISM heating source to the west. This can be seen also in Fig. 7g–h, which show an intensification of the causal effect of the ISM convection on potential temperature over the middle east area, thus highlighting the presence of diabatic heating (adiabatic heating would not cause a change in potential temperature).

The Middle East ridge is also closely connected to the circumglobal teleconnection pattern (Ding and Wang 2005; Di Capua et al. 2020a). This connection can be seen in the causal effect networks in Fig. 3c, d, which depict a strong positive two-way causal link between the circumglobal teleconnection (CGT) index and the ME-ridge at 3-day time scale (Fig. 3c), evolving in a one-way positive link from the CGT index to the ME-ridge at weekly time scale (Fig. 3d). Thus, this puts the ME-ridge in direct connection with the two-way causal link between the ISM convective activity and the CGT index which was shown in Di Capua et al. (2020a). In this context, the CGT index and the monsoon desert mechanisms are both affected by ISM convection, but the northward location of the CGT index region (east of the Caspian Sea), allows the influence of the ISM to reach the mid-latitude circulation. It is interesting to notice that the North Atlantic wave as defined in Fig. 2g has a negative effect on the ME-ridge at 3-day time scale and on CGT index at weekly time scales. This introduces a negative feedback inside the Etesian CEN: while the North Atlantic wave has a positive causal effect on the Etesians (i.e. a stronger wave leads to more enhanced Etesians), its effect on the ME-ridge (or CGT index) is negative, thus a stronger wave weakens the Middle East ridge, and in turn, with a delayed effect, the Etesians. This behaviour can be seen in the correlation maps between the Etesians and Z200 fields shown in Fig. 2m: when the NAtl-wave propagates eastward, it is associated with negative Z200 anomalies over the ME-region.

Analysing the stationarity in time of the causal effect networks shows that the sign and direction of the causal links is stable over time (Fig. S9). The link from the North Atlantic wave to the Etesians shows a weakening over the analysed time period. The presence of this weakening trend implies that the influence of the mid-latitude circulation on the eastern Mediterranean circulation may decrease over the years, leaving the Etesians more subject to the influence of the ISM system. Determining the cause of this trend is outside the scope of this paper. Moreover, future projections show a strengthening of the ISM precipitation (Turner and Annamalai 2012; Menon et al. 2013), due to the increased water vapor holding capacity of the atmosphere with increasing temperatures, which may lead to an intensification of the monsoon – desert mechanisms. This provides the potential for an increased influence of the ISM convection on the eastern Mediterranean circulation. In general, more intense Indian monsoon rainfall would lead to a stronger Middle East ridge and, thus, stronger Etesians. If true, due to the link between Etesians and surface temperatures, this may have a mitigating effect on heat waves in the area.

In conclusion, in this work we quantify the relative importance of mid-latitude and tropical causal drivers in

influencing the intraseasonal variability of Etesians winds and tropospheric circulation in the eastern Mediterranean. Our results highlight the importance of different time scales and show that the tropical influence of monsoon convective activity, which is mediated by the Middle East ridge, becomes more prominent than that of mid-latitude drivers at longer time scales (weekly versus 3-day time steps). Moreover, we show how the heat low that characterises the circulation over the Middle East in summer is established as a consequence of the upper level ridge, which in turn is caused by the heat source provided by the Indian monsoon. In contrast, an influence of the mid-latitude wave on the heat low is not detected. Our results support that this Indian monsoon–Middle East pathway is embedded in the monsoon–desert mechanism and that changes in the circulation over the eastern Mediterranean are closely related to changes in tropical convective activity. Finally, we show that the causal discovery tool employed can shed light on dynamical pathways in reanalysis datasets, thus constituting a useful tool for process-based validation of general circulation models. Future work will assess how these causal pathways will change under global warming and what impact these changes will have on surface temperature and fire weather in the region.

Supplementary Information The online version supplementary material available at https://doi.org/10.1007/s00382-024-07411-y.

Acknowledgements We thank the two anonymous reviewers for their insightful and sensible suggestions, which have helped us to improve the quality of the analysis and the clarity of the manuscript.

Author contributions All authors contributed to the study conception and design. Material preparation, data collection and analysis were performed by Giorgia Di Capua. The first draft of the manuscript was written by Giorgia Di Capua and all authors commented on previous versions of the manuscript. All authors read and approved the final manuscript.

Funding Open Access funding enabled and organized by Projekt DEAL. The research leading to these results has received funding from the German Federal Ministry of Education and Research (BMBF) through the JPI Climate/JPI Oceans NextG-Climate Science project ROADMAP (grant no. 01LP2002B, G.D.C. and R.V.D.; grant no. 01LP2002A, D.M.), the HORIZON-RIA project PREVENT (grant no. 101081276; G.D.C.), the EU Horizon Project Impetus4Change (Grant Agreement no. 101081555) (D.M.) and the German Academic Exchange Service (DAAD, grant no. 57628437; G.D.C and R.V.D.).

Data availability The data used in this article can be accessed by contacting the corresponding author. ERA5 (https://doi.org/10.24381/cds.50ed0a73, Copernicus Climate Change Service, Climate Data Store, 2018) datasets are publicly available on the Copernicus website.

Declarations

Conflict of interest The contact author has declared that none of the authors has any competing interests.

Open Access This article is licensed under a Creative Commons Attribution 4.0 International License, which permits use, sharing, adaptation, distribution and reproduction in any medium or format, as long as you give appropriate credit to the original author(s) and the source, provide a link to the Creative Commons licence, and indicate if changes were made. The images or other third party material in this article are included in the article's Creative Commons licence, unless indicated otherwise in a credit line to the material. If material is not included in the article's Creative Commons licence and your intended use is not permitted by statutory regulation or exceeds the permitted use, you will need to obtain permission directly from the copyright holder. To view a copy of this licence, visit http://creativecommons.org/licenses/by/4.0/.

References

Barcikowska MJ, Kapnick SB, Krishnamurty L et al (2020) Changes in the future summer Mediterranean climate: contribution of teleconnections and local factors. Earth Syst Dyn 11:161–181. https://doi.org/10.5194/esd-11-161-2020

Benjamini Y, Hochberg Y (1995) Controlling the false discovery rate: a practical and powerful approach to multiple testing. J R Stat Soc Ser B 57:289–300. https://doi.org/10.2307/2346101

Branstator G (2014) Long-lived response of the midlatitude circulation and storm tracks to pulses of tropical heating. J Clim 27:8809–8826. https://doi.org/10.1175/JCLI-D-14-00312.1

Cherchi A, Annamalai H, Masina S, Navarra A (2014) South Asian summer monsoon and the eastern Mediterranean climate: the monsoon-desert mechanism in CMIP5 simulations. J Clim 27:6877–6903. https://doi.org/10.1175/JCLI-D-13-00530.1

Cherchi A, Annamalai H, Masina S et al (2016) Twenty-first century projected summer mean climate in the Mediterranean interpreted through the monsoon-desert mechanism. Clim Dyn 47:2361–2371. https://doi.org/10.1007/s00382-015-2968-4

Di Capua G, Kretschmer M, Donner RV et al (2020a) Tropical and mid-latitude teleconnections interacting with the Indian summer monsoon rainfall: a theory-guided causal effect network approach. Earth Syst Dyn 11:17–34. https://doi.org/10.5194/esd-11-17-2020

Di Capua G, Runge J, Donner RV et al (2020b) Dominant patterns of interaction between the tropics and mid-latitudes in boreal summer: causal relationships and the role of timescales. Weather Clim Dyn 1:519–539. https://doi.org/10.5194/wcd-1-519-2020

Di Capua G, Coumou D, van der Hurk B et al (2023) Validation of boreal summer tropical-extratropical causal links in seasonal forecasts. Weather Clim Dyn 4:701–723

Ding Q, Wang B (2005) Circumglobal teleconnection in the Northern Hemisphere summer. J Clim 18:3483–3505. https://doi.org/10.1175/JCLI3473.1

Ezber Y (2019) Assessment of the changes in the Etesians in the EURO-CORDEX regional model projections. Int J Climatol 39:1213–1229. https://doi.org/10.1002/joc.5872

Founda D, Santamouris M (2017) Synergies between Urban Heat Island and Heat Waves in Athens (Greece), during an extremely hot summer (2012). Sci Rep 7:1–11. https://doi.org/10.1038/s41598-017-11407-6

Gadgil S, Joseph PV (2003) On breaks of the Indian monsoon. Proc Indian Acad Sci (Earth Planet Sci) 112:529–558. https://doi.org/10.1007/BF02709778

Gasparrini A, Guo Y, Sera F et al (2017) Projections of temperature-related excess mortality under climate change scenarios. Lancet Planet Health 1:e360–e367. https://doi.org/10.1016/S2542-5196(17)30156-0

Grillakis MG (2019) Increase in severe and extreme soil moisture droughts for Europe under climate change. Sci Total Environ 660:1245–1255. https://doi.org/10.1016/j.scitotenv.2019.01.001

Hersbach H, Bell B, Berrisford P et al (2020) The ERA5 global reanalysis. Q J R Meteorol Soc 146:1999–2049. https://doi.org/10.1002/qj.3803

Hlinka J, Hartman D, Jajcay N et al (2014) Nonlinear processes in geophysics regional and inter-regional effects in evolving climate networks. Nonlinear Process Geophys. https://doi.org/10.5194/npg-21-451-2014

Hochman A, Marra F, Messori G et al (2022) Extreme weather and societal impacts in the eastern Mediterranean. Earth Syst Dyn 13:749–777. https://doi.org/10.5194/esd-13-749-2022

Jiang X, Li T, Wang B (2004) Structures and mechanisms of the northward propagating boreal summer intraseasonal oscillation. J Clim 17:1022–1039. https://doi.org/10.1175/1520-0442(2004)017%3c1022:SAMOTN%3e2.0.CO;2

Kanakidou M, Mihalopoulos N, Kindap T et al (2011) Megacities as hot spots of air pollution in the East Mediterranean. Atmos Environ 45:1223–1235. https://doi.org/10.1016/j.atmosenv.2010.11.048

Katzenberger A, Schewe J, Pongratz J, Levermann A (2021) Robust increase of Indian monsoon rainfall and its variability under future warming in CMIP6 models. Earth Syst Dyn 12:367–386. https://doi.org/10.5194/esd-12-367-2021

Kelley CP, Mohtadi S, Cane MA et al (2015) Climate change in the Fertile Crescent and implications of the recent Syrian drought. Proc Natl Acad Sci USA 112:3241–3246. https://doi.org/10.1073/pnas.1421533112

Kikuchi K, Wang B, Kajikawa Y (2012) Bimodal representation of the tropical intraseasonal oscillation. Clim Dyn 38:1989–2000. https://doi.org/10.1007/s00382-011-1159-1

Kretschmer M, Coumou D, Donges JF, Runge J (2016) Using causal effect networks to analyze different Arctic drivers of mid-latitude winter circulation. J Clim 29:4069–4081. https://doi.org/10.1175/JCLI-D-15-0654.1

Kretschmer M, Runge J, Coumou D (2017) Early prediction of extreme stratospheric polar vortex states based on causal precursors. Geophys Res Lett 44:8592–8600. https://doi.org/10.1002/2017GL074696

Kretschmer M, Cohen J, Matthias V et al (2018) The different stratospheric influence on cold-extremes in Eurasia and North America. npj Clim Atmos Sci 1:1–10. https://doi.org/10.1038/s41612-018-0054-4

Kulkarni A, Kripalani R, Sabade S, Rajeevan M (2011) Role of intra-seasonal oscillations in modulating Indian summer monsoon rainfall. Clim Dyn 36:1005–1021. https://doi.org/10.1007/s00382-010-0973-1

Lehmann J, Kretschmer M, Schauberger B, Wechsung F (2020) Potential for early forecast of Moroccan wheat yields based on climatic drivers. Geophys Res Lett 47:e2020GL087516. https://doi.org/10.1029/2020GL087516

Menon A, Levermann A, Schewe J et al (2013) Consistent increase in Indian monsoon rainfall and its variability across CMIP-5 models. Earth Syst Dyn 4:287–300. https://doi.org/10.5194/esd-4-287-2013

Metaxas DA, Bartzokas A (1994) Pressure covariability over the Atlantic, Europe and N. Africa application: centers of action for temperature, winter precipitation and summer winds in Athens, Greece. Theor Appl Climatol 49:9–18. https://doi.org/10.1007/BF00866284

Morán-Ordóñez A, Duane A, Gil-Tena A et al (2020) Future impact of climate extremes in the Mediterranean: soil erosion projections when fire and extreme rainfall meet. Land Degrad Dev 31:3040–3054. https://doi.org/10.1002/ldr.3694

Nowack P, Runge J, Eyring V, Haigh JD (2020) Causal networks for climate model evaluation and constrained projections. Nat Commun 11:1415. https://doi.org/10.1038/s41467-020-15195-y

Paschalidou AK, Kassomenos PA (2016) What are the most fire-dangerous atmospheric circulations in the Eastern-Mediterranean? Analysis of the synoptic wildfire climatology. Sci Total Environ 539:536–545. https://doi.org/10.1016/j.scitotenv.2015.09.039

Pfleiderer P, Schleussner C-F, Geiger T, Kretschmer M (2020) Robust predictors for seasonal Atlantic hurricane activity identified with causal effect networks. Weather Clim Dyn 1:313–324. https://doi.org/10.5194/wcd-1-313-2020

Poupkou A, Zanis P, Nastos P et al (2011) Present climate trend analysis of the Etesian winds in the Aegean Sea. Theor Appl Climatol 106:459–472. https://doi.org/10.1007/s00704-011-0443-7

Raicich F, Pinardi N, Navarra A (2003) Teleconnections between Indian monsoon and Sahel rainfall and the Mediterranean. Int J Climatol 23:173–186. https://doi.org/10.1002/joc.862

Rajeevan M, Gadgil S, Bhate J (2010) Active and break spells of the Indian summer monsoon. J Earth Syst Sci 119:229–247. https://doi.org/10.1007/s12040-010-0019-4

Rizos K, Logothetis I, Koukouli ME et al (2022) The influence of the summer tropospheric circulation on the observed ozone mixing ratios at a coastal site in the Eastern Mediterranean. Atmos Pollut Res 13:101381. https://doi.org/10.1016/j.apr.2022.101381

Rodwell MJ, Hoskins B (1996) Monsoons and the dynamics of deserts. Q J R Meteorol Soc 122:1385–1404

Rodwell MJ, Hoskins BJ (2001) Subtropical anticyclones and summer monsoons. J Clim 14:3192–3211. https://doi.org/10.1175/1520-0442(2001)014%3c3192:SAASM%3e2.0.CO;2

Ruffault J, Curt T, Martin-Stpaul NK et al (2018) Extreme wildfire events are linked to global-change-type droughts in the northern Mediterranean. Nat Hazards Earth Syst Sci 18:847–856. https://doi.org/10.5194/nhess-18-847-2018

Runge J (2018) Causal network reconstruction from time series: from theoretical assumptions to practical estimation. Chaos 28:075310. https://doi.org/10.1063/1.5025050

Runge J, Petoukhov V, Kurths J (2014) Quantifying the strength and delay of climatic interactions: the ambiguities of cross correlation and a novel measure based on graphical models. J Clim 27:720–739. https://doi.org/10.1175/JCLI-D-13-00159.1

Runge J, Nowack P, Kretschmer M et al (2019) Detecting causal associations in large nonlinear time series datasets. Sci Adv 5:eaau4996

Schleussner C, Donges JF, Donner RV, Joachim H (2016) Armed-conflict risks enhanced by climate-related disasters in ethnically fractionalized countries. Proc Natl Acad Sci USA. https://doi.org/10.1073/pnas.1601611113

Seager R, Liu H, Henderson N et al (2014) Causes of increasing aridification of the Mediterranean region in response to rising greenhouse gases. J Clim 27:4655–4676. https://doi.org/10.1175/JCLI-D-13-00446.1

Stephan CC, Klingaman NP, Turner AG (2019) A mechanism for the interdecadal variability of the Silk Road Pattern. J Clim 32:717–736. https://doi.org/10.1175/JCLI-D-18-0405.1

Suhas E, Neena JM, Goswami BN (2012) Interannual variability of Indian summer monsoon arising from interactions between seasonal mean and intraseasonal oscillations. J Atmos Sci 69:1761–1774. https://doi.org/10.1175/JAS-D-11-0211.1

Turner AG, Annamalai H (2012) Climate change and the south Asian summer monsoon. Nat Clim Chang. https://doi.org/10.1038/NCLIMATE1495

Tyrlis E, Lelieveld J (2013) Climatology and dynamics of the summer Etesian winds over the eastern Mediterranean. J Atmos Sci 70:3374–3396. https://doi.org/10.1175/JAS-D-13-035.1

Tyrlis E, Lelieveld J, Steil B (2013) The summer circulation over the eastern Mediterranean and the Middle East: influence of the

South Asian monsoon. Clim Dyn 40:1103–1123. https://doi.org/10.1007/s00382-012-1528-4

Tyrlis E, Tymvios FS, Giannakopoulos C, Lelieveld J (2015) The role of blocking in the summer 2014 collapse of Etesians over the Eastern Mediterranean. J Geophys Res 120:6777–6792. https://doi.org/10.1002/2015JD023543

Vijverberg S, Schmeits M, van der Wiel K, Coumou D (2020) Subseasonal statistical forecasts of eastern U.S. hot temperature events. Mon Weather Rev 148:4799–4822. https://doi.org/10.1175/MWR-D-19-0409.1

Vijverberg S, Coumou D (2022) The role of the Pacific Decadal Oscillation and ocean-atmosphere interactions in driving US temperature variability. npj Clim Atmos Sci 5:18. https://doi.org/10.1038/s41612-022-00237-7

Vogel MM, Hauser M, Seneviratne SI (2020) Projected changes in hot, dry and wet extreme events' clusters in CMIP6 multi-model ensemble. Environ Res Lett 15:094021. https://doi.org/10.1088/1748-9326/ab90a7

Wang B, Jin C, Liu J (2020) Understanding future change of global monsoons projected by CMIP6 models. J Clim 33:6471–6489. https://doi.org/10.1175/JCLI-D-19-0993.1

Ziv B, Saaroni H, Alpert P (2004) The factors governing the summer regime of the eastern Mediterranean. Int J Climatol 24:1859–1871. https://doi.org/10.1002/joc.1113

Publisher's Note Springer Nature remains neutral with regard to jurisdictional claims in published maps and institutional affiliations.